KU LEUVEN

FACULTY OF SCIENCE

Lattice site and thermal stability of transition metals in germanium

Valérie AUGUSTYNS

Supervisor: Prof. A. Vantomme

Co-supervisor: Dr. L. Pereira

Thesis presented in
fulfillment of the requirements
for the degree of Master of Science
in Physics

Academic year 2012-2013

Dankwoord

Een masterthesis is als de kers op een taart voor een opleiding. Het is als het ware een werk dat - jammer genoeg - het einde afkondigt van een 5 jaar durende vorming in de wondere wereld van de fysica alsook in de zoektocht naar mezelf. Natuurlijk ben ik niet alleen door deze periode gegaan, dus bij deze zou ik graag een aantal mensen in de bloemtjes zetten.

Eerst en vooral wil ik graag specifiek de mensen bedanken die mij geholpen hebben met het tot stand brengen van mijn masterthesis. Bij mijn promoter prof. A. Vantomme kon ik terecht voor zeer veel praktische zaken. Hij heeft mij ook heel goed geleerd hoe ik dit werk een logische opbouw kon bezorgen. Maar ook een fysische input kon ik van hem zeker ontvangen. Aangezien het ook belangrijk is om je bedenkingen met verschillende mensen te kunnen bespreken, heb ik naast mijn promotor ook met anderen ideeën uitgewisseld.
Door Dr. Stefan Decoster kwam ik voor het eerst in contact met de emission channeling techniek alsook met germanium. Zelfs na zijn vertrek na het eerste semester, kon ik nog steeds bij hem terecht met vragen via mail, waarvan de antwoorden me elke keer opnieuw weer een stuk verder brachten!
After a first short literature study, I left to Lisbon (Portugal) for one semester. My time in Lisbon was a very great experience. I learned a lot about myself, the Portuguese culture, but I also met Dr. Ulrich Walh, alias Uli. He helped me with a very large part of the analysis and answered a large amount of "lattice site location" questions on our weekly appointments.
No doubt, the biggest breakthrough was my emission channeling experience in CERN in the end of November. Over there, Uli and Dr. Lino da Costa Pereira teached me so much whereby a lot of missing puzzle pieces were found for me. Especially Lino helped with all the paperwork that was involved in my stay over there.
After my Portuguese adventure, my co-promoter Lino answered all my questions. I also really want to thank him for finding the time to read and correct the draft version(s) this work. Also Lígia helped me with some calculations.

Naast de mensen die mij heel erg geholpen hebben met het begrijpen van de fysica die nodig was om deze masterproef tot een goed einde te brengen, zijn toch ook zeker mijn mede-jaargenoten belangrijk geweest voor mij. 's Middags om stipt 12u samen in de Moete gaan eten om dan even er tussen uit te zijn, helpt toch om er

nadien weer met volle moed aan te kunnen beginnen. In het bijzonder wil ik graag Janne bedanken waarmee ik de voorbije jaren vaak mee samen heb gewerkt; we waren nog al eens een team!
Ontspanning is ook heel belangrijk, daarom ben ik heel blij dat ik af en toe mijn hoofd eens kon leegmaken bij één van mijn vele hobby's. Tijdens de jazzdance kon ik even alles van mij af dansen en tijdens de gitaarkwartetlessen kwam ik dan weer helemaal tot rust. Maar de beste ontspanning was toch om te kunnen gaan "ravotten" op zaterdagnamiddag bij de gidsen van Sint-Godelieve. Tijdens de zomer - als kroonwerk op het jaar - 10 dagen op kamp vol avontuur, plezier en weinig slaap; een bijzondere combinatie.

Ik vind het ook belangrijk om mijn ouders en mijn broer(tje) in de verf te zetten. De voorbije jaren vormden een enorm woelige periode, maar mama, Martijn en de paps, jullie probeerden toch steeds aanwezig te zijn.
Tenslotte moet ik toch nog zeker Bart enorm bedanken. Hij is de laatste jaren enorm belangrijk geweest om mij voor de zoveelste keer weer moed in te spreken. Altijd kon ik op hem rekenen! Het afgelopen jaar heeft ook zijn mama mij vaak een hart onder de riem gestoken.

Bedankt!

Valérie Augustyns,
Leuven, juni 2013

Nederlandstalige samenvatting

Ondanks dat de eerste transistor germanium als basismateriaal gebruikte, is de elektronicatechnologie de dag van vandaag gebaseerd op silicium. Dit is het gevolg van een grotere aanwezigheid, een lagere prijs en een betere kwaliteit van de silicium-oxide tegenover germanium. De voordelen (bijvoorbeeld een hogere mobiliteit van de ladingsdragers) van germanium tegenover silicium geven een motivatie om meer onderzoek naar germanium gebaseerde materialen te verrichten.

De dopering van halfgeleiders (bijvoorbeeld door de introductie van onzuiverheden in silicium en germanium, waardoor hun eigenschappen kunnen gewijzigd en gecontroleerd worden) kan gebeuren via de implantatie van ionen of door de invoeging van de doperingsatomen gedurende de groei van de halfgeleider. In deze masterproef werd ionenimplantatie gebruikt. De implantatie als ook de daaropvolgende metingen werden in ISOLDE (CERN) uitgevoerd, waarbij gebruik werd gemaakt van de emissie kanalisatietechniek. Ionenimplantatie creëert ongewenste defecten (bijvoorbeeld vacatures) in het basismateriaal. Deze geïntroduceerde defecten kunnen gereduceerd worden door een verhoogde temperatuur gedurende de implantatie te gebruiken. Voor deze masterproef werden overgangsmetalen geïmplanteerd. In tegenstelling tot onzuiverheden van groep III (bijvoorbeeld boor) en V (bijvoorbeeld fosfor), die zich gedragen als elektrische doperingsatomen, leidt de introductie van overgangsmetalen in germanium tot energieniveaus rond het midden van de bandkloof, waardoor die zich gedragen als *elektrische* compensatie-defecten. Anderzijds kunnen overgangsmetalen in niet-magnetische halfgeleiders, zoals germanium, ingevoegd worden om een *magnetisch* gedrag te induceren. Deze materialen (zoals mangaan gedopeerd germanium) worden ook wel verdunde magnetische halfgeleiders (DMS) genoemd. Zowel de elektrische als de magnetische eigenschappen van onzuiverheden zijn sterk afhankelijk van de ingenomen roosterlocatie. Ondanks dat het gedrag van substitutionele (S) onzuiverheden (zoals overgangsmetalen op een oorspronkelijk ingenomen germaniumpositie) relatief goed gekend is, zijn interstitiële overgangsmetalen minder goed begrepen.

In dit werk werden de roosterlocaties van geïmplanteerd mangaan en nikkel in germanium onderzocht. Naast substitutionele locaties, werden ook interstitiële locaties ingenomen. De tot nu toe onderzochte 3d overgangsmetalen in germanium hebben op zijn minst een fractie van de onzuiverheden op de nabij-BC positie. De BindingsCentrum locatie is gelegen tussen twee dichtstbijzijnde substitutionele posities (langs de $< 111 >$

richting). Deze locatie is gerelateerd aan een onzuiverheid-vacature-complex, dat ook wel de gesplitste-vacature configuratie wordt genoemd. Wanneer een onzuiverheid op de substitutionele positie één van de beschikbare vacatures vangt, dan zal de onzuiverheid spontaan naar de BC positie gaan. De fractie van de overgangsmetalen op de S en op de nabij-BC positie varieert respectievelijk tussen 20% en 40% en tussen 20% en 30%. Voor het experiment waarbij nikkel geïmplanteerd werd in germanium, bevinden $19 \pm 3\%$ van de nikkel atomen zich op een andere interstitiële positie, een tetrahedrale (T) locatie met een grote *rms* (*root-mean-square*) verplaatsing. In deze masterproef wordt gesuggereerd dat deze tetrahedrale interstitiële positie gerelateerd is aan defectcomplexen.

Deze roosterlocaties werden bekomen voor verschillende uitgloeitemperaturen. Voor de tot hiertoe onderzochte 3d transitiemetalen is de S locatie stabiel tot op 350°C en de nabij-BC locatie tot op 300°C. Voor mangaan in germanium dalen de fracties in functie van een stijgende uitgloeitemperatuur. Waarschijnlijk is dit het gevolg van de diffusie van defecten gedurende de uitgloeiing, die hierdoor de mogelijkheid krijgen om mangaanatomen op te nemen in wanordelijke regio's. Bijgevolg zijn er nadien minder mangaanatomen te vinden op locaties die een hoge symmetrie vertonen. Wanneer nikkel geïmplanteerd wordt in germanium stijgen eerst de fracties tot een temperatuur van 350°C ten gevolge van het herstel van de implantatieschade door de uitgloeiing. Daarna dalen de fracties omwille van inwaartse lange afstandsdiffusie of door clustering.

Ter conclusie is het belangrijk om te vermelden dat naast substitutionele posities, ook nabij-BC locaties ingenomen werden door de 3d overgangsmetalen die tot hiertoe al onderzocht zijn in germanium. Voor mangaan in germanium zijn deze studies interessant voor de toepassing in verdunde magnetische halfgeleiders, aangezien het magnetisch gedrag van de magnetische doperingsatomen sterk afhankelijk is van de ingenomen roosterlocatie. Het nikkel in germanium experiment, dat het eerste emissie kanalisatie experiment was dat gebruik maakte van een nikkelisotoop, vertoonde een onverwachte bezetting van een interstitiële locatie (de T positie met een grote *rms* verplaatsing).

Summary

Although the first transistor was based on germanium, current chip technology mainly uses silicon due to its larger abundance, a lower price and higher quality silicon-oxide. However, a very important goal in microelectronics is to obtain faster integrated circuits. The advantages of germanium compared to silicon (e.g. a higher mobility of the charge carriers) motivates further research on germanium based materials.

Semiconductor doping (e.g. introducing impurities into silicon and germanium in order to alter - and control - their properties) can be done by ion implantation or by in situ doping, whereby the host material is doped during growth. This thesis focusses on introducing dopants by ion implantation. The implantation as well as the subsequent measurements were performed in ISOLDE (CERN) using the emission channeling technique. Although ion implantation generates undesired defects in the host material (e.g. vacancies), such damage can be reduced by performing the implantation at an elevated temperature. In this thesis, the implanted ions are transition metals. In contrast to elements from group III (e.g. boron) and V (e.g. phosphorus), which act as electrical dopants, transition metal impurities in germanium introduce deep levels around the middle of the band gap, and therefore can act as compensating *electrical* defects. On the other hand, transition metals may be incorporated in non-magnetic semiconductors such as germanium to induce *magnetic* behaviour. Such materials, e.g. manganese doped germanium, are known as dilute magnetic semiconductors (DMS). Both electric and magnetic properties of transition metal impurities strongly depend on the occupied lattice sites. Although the behaviour of substitutional (S) impurities (i.e. transition metals on an originally occupied germanium position) is relatively well established, interstitial transition metals are poorly understood.

In this work, we studied the lattice site of manganese and nickel implanted in germanium. It was observed that apart from substitutional locations, also interstitial positions were occupied. All the investigated 3d transition metals in germanium had at least a fraction of the impurities located at a near-bond-centered (BC) position. This BC site is located between two nearest neighbouring S sites (along the $< 111 >$ direction) and is related to an impurity-vacancy-complex or the split-vacancy configuration. When an impurity on the substitutional site traps one vacancy which is available due to the implantation process, the impurity spontaneously evolves to the BC site. The fraction of transition metals on the S site and on the near-BC location varied from 20% to 40% and from 20%

to 30% respectively. In as-implanted nickel in germanium, 19±3% of the nickel atoms occupied an additional interstitial site: a T site with a large root-mean-square (*rms*) displacement. This tetrahedral site was interpreted to be related to defect complexes.

The lattice sites were determined for different annealing temperatures. The S site was found to be stable up to at least 350°C and the near-BC site up to 300°C for the investigated 3d transition metals. For manganese in germanium, the fitted fractions decrease as a function of increasing annealing temperature. This is likely due to the diffusion of defects during annealing, which are able to trap manganese atoms in disordered regions. This causes a decreasing amount of manganese atoms on high symmetry sites. When nickel was implanted in germanium, the fractions initially increased up to an annealing temperature of 350°C, whereby the annealing causes a recovery of the lattice structure. Afterwards, the fractions decreased, which we interpret as being due to clustering or inward long range diffusion.

In conclusion, apart from substitutional locations, also near-BC sites are occupied for the already investigated 3d transition metals (manganese, iron, nickel and copper) in germanium. For manganese in germanium, these results are particularly interesting in the context of dilute magnetic semiconductors, since the magnetic behaviour of magnetic dopants strongly depends on the occupied lattice sites. The experiment on nickel in germanium, which constituted the first emission channeling measurement making use of a nickel isotope, showed the occupation of an unexpected interstitial site (the T site with a large rms displacement).

Content

Dankwoord iii

Nederlandstalige samenvatting v

Summary vii

1 Introduction 1
- 1.1 Germanium . . . 1
  - 1.1.1 Historical context . . . 1
  - 1.1.2 Germanium lattice . . . 2
- 1.2 Transition metals in germanium . . . 3
  - 1.2.1 Properties . . . 4
    - 1.2.1.1 Electrical properties . . . 4
    - 1.2.1.2 Magnetic properties . . . 5
    - 1.2.1.3 Diffusivity: diffusion mechanisms . . . 6
    - 1.2.1.4 Solubility . . . 10
  - 1.2.2 Lattice site location . . . 10
- 1.3 Ion implantation: production of defects . . . 12
  - 1.3.1 Native defects . . . 13
  - 1.3.2 Impurity-related defects . . . 14
- 1.4 Goals . . . 16

2 Electron emission channeling 17
- 2.1 Electron emission . . . 18
- 2.2 Electron channeling . . . 18
- 2.3 Experimental set-up . . . 21
  - 2.3.1 Ion implantation: ISOLDE in CERN . . . 22
  - 2.3.2 Electron emission channeling set-up . . . 24
- 2.4 Data analysis . . . 28
  - 2.4.1 Fitting procedure . . . 28
  - 2.4.2 Correction factors . . . 30

3 Experimental results and discussion 32

3.1 Manganese in germanium 33
3.1.1 Experimental details 33
3.1.2 Results 33
3.1.3 Summary about Mn in Ge 38
3.2 Nickel in germanium 39
3.2.1 Experimental details 39
3.2.2 Results 39
3.2.3 Summary about Ni in Ge 44
3.3 Comparison of different transition metals in Ge 45

4 Conclusions and outlook **50**

Bibliography **52**

Chapter 1

Introduction

In this thesis, transition metals are introduced in germanium using ion implantation. To start, this chapter gives an introductory overview of the properties of the host material, germanium (Ge). Afterwards, the impurities which were implanted in the Ge lattice are highlighted. Therefore, a number of electrical and magnetic properties of manganese, nickel, copper and iron in germanium are reviewed. Also the different types of diffusion mechanisms are discussed. In addition, the different possible high symmetry sites in Ge for these transition metals are displayed. These lattice site location studies are of interest, because the functional properties of semiconductors strongly depend on the position of the impurities in the host material. It is also illustrated that some defect-related configurations have a preference for a particular lattice site. Finally, an overview of the goals concludes this thesis.

1.1 Germanium

1.1.1 Historical context

Germanium (Ge) was discovered in 1886 by C. Winkler [1]. Although silicon (Si) had been discovered 66 years before, the first transistor and integrated circuit developments used Ge as a basic compound [2]. In these semiconductor transistors, the highest achievable crystalline quality at that time was obtained with Ge [3]. However, after some time, disadvantages of Ge emerged. First of all, it was not possible to obtain sufficient surface passivation by using germanium-oxide (GeO_2) due to its low quality [4].

A funny story can be told about the first bipolar junction transistor, which used Ge as a main compound [5]. This type of device was used in transistor radios by Motorola Corporation in 1955 [6]. There was one major problem: when the cars were parked under the hot summer, the radios didn't work any more. This was due to the relative small band gap of Ge (compared to the one of silicon), which leads to an intrinsic behaviour of Ge at these higher temperatures. Because of this, the n-type and p-type regions lost their proper properties and therefore, the radios stopped working.

In the beginning of the sixties, it turned out that the behaviour of SiO_2 was by far better compared to germanium-oxide. Si also had a larger abundance, and therefore a lower price [2]. Because of this and the start of the planar technology on silicon wafers [7], microelectronics became Si based. In the past years, it is important in microelectronics to follow the law of Moore, i.e. to double the number of transistors on a integrated circuit every two years.
In order to pursue this exponential improvement, Ge offers some benefits over Si. In Ge, the free charge carriers have a higher mobility and due to the lower band gap compared to Si, the dopants have a lower activation temperature [8]. These properties are needed to obtain faster integrated circuits.
Other advantages of Ge are used in some niche markets [2]. In nuclear physics, X- and γ-ray detectors take advantage of a high stopping power to electromagnetic radiation and the ability to grow Ge into large single crystals containing very low impurity concentrations. Apart from these specific places where Ge has already been used for a long time, more research is needed to possibly apply Ge in the microelectronic technology, which is dominated by Si until now.

1.1.2 Germanium lattice

In order to know where impurities will reside when they are implanted in a Ge crystal, the first step is to identify how the host lattice looks like. An ideal intrinsic Ge lattice can be characterized by a face-centered cubic crystal structure (see figure 1.1) with a Fd-3m space group. In this ideal unit cell, all the Ge atoms are located at substitutional positions. Si atoms also occupy this diamond lattice structure. For Ge, the unit cell has a dimension of 5.66 x 5.66 $Å^3$.

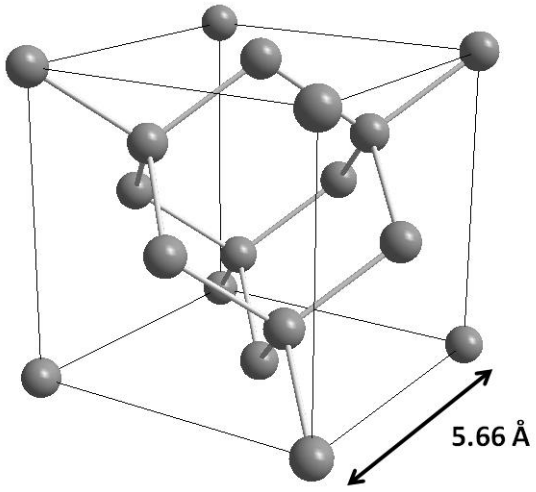

FIGURE 1.1: Unit cell of a germanium lattice, made by Diamond3 software

1.2 Transition metals in germanium

Different types of impurities may be used for Ge doping. The best known dopants in semiconductor applications are the ones from group III and V, which act as electrical dopants [9]. An n-type semiconductor is obtained by incorporating a donor impurity from group V, which occupies a substitutional site, whereby a donor level is created just below the conduction band. In order to obtain an acceptor level just above the valence band (for p-type doping), a group III impurity can be added to the Ge lattice. Apart from these most investigated electrical dopants, other impurity elements exhibit properties of interest for different applications. Transition metals with an incomplete d sub-shell (e.g. 3d transition metals) are a good example of that. The most investigated transition metal in Ge is copper (Cu). Cu-doped Ge detectors are used in experimental nuclear physics [10]. In addition, Cu is used to form low resistivity phases at relatively low temperatures (150° - 360°C) in Ge-based microelectronic applications [11]. For the use in ohmic contact element, even more interesting properties can be obtained by using nickel (Ni) instead of Cu. NiGe has a low resistivity and formation temperature. This together with its sufficiently morphological stability and limited sensitivity to oxidation makes Ni in Ge a promising low resistivity contact [11]. Transition metal dopants also have interesting magnetic properties [12]. For example, Mn doped Ge is an intensively investigated dilute magnetic semiconductor (DMS).

In the following section, the electric and magnetic behaviour of transition metals in Ge are briefly discussed in order to illustrate the importance of lattice site location studies. Also the diffusion mechanisms and the concept of solubility are described.

1.2.1 Properties

1.2.1.1 Electrical properties

A very important difference between dopants from group III and V compared to transition metals is the location of the energy levels in the band gap of Ge (0.67 eV at a temperature of 29°C [13]). When the energy levels are just below the conduction band or just above the valence band (around 0.1 eV difference), the dopants are shallow impurities (e.g. elements from group III and V). However, energy levels near the middle of the band gap are introduced for transition metals in germanium [9]. These deep impurities can act as traps for the charge carriers. The traps can capture an electron or a hole, but eventually after the trapping, the carrier goes back to the band from where it came. However, this time delay is large enough to withhold the carrier to contribute to the measured pulse. Another possible characteristic of deep levels is to act as recombination centers, where an electron and a hole are able to annihilate. The overall effect of such deep impurities is the decrease in charge carrier concentration.
For impurities that occupy a substitutional site inside the lattice, i.e. a replacement of a Ge lattice atom, the number of energy levels inside the band gap is explained by the tetrahedral bonding model [14]. This model makes the connection between the electron configuration of the dopant and the number of energy levels inside the band gap. The valence electrons of a Ge atom occupy the $4s^2 4p^2$ configuration, therefore, four bondings to neighbouring atoms can be established. A Mn, Ni or Fe atom contains only 2 electrons in the outer s-shell. Therefore, these atoms have a deficit of two electrons from the four nearest neighbour Ge atoms and they will act as double acceptors. Cu has a $4s^1$ configuration for its valence electrons and that is why it behaves as a triple acceptor.
The energy levels in the band gap of Ge are shown in figure 1.2. The number of levels and the acceptor nature were also experimental investigated. By measuring the temperature dependency of the electrical resistivity and Hall coefficient in p-type and n-type Mn-doped Ge crystals, the two acceptor levels due to the introduction of Mn in Ge were confirmed [15]. The same type of experiments also described the two level acceptor behaviour of Ni in Ge [16].

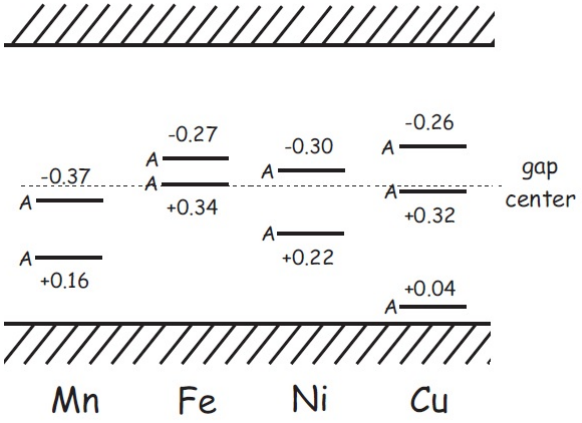

FIGURE 1.2: Schematic view of the deep acceptor levels in germanium. The dashed line is the gap center. If the energy value (in eV) is positive, the value is given relative to the valence band. Otherwise, with a negative energy value, it is relative to the conduction band [2, 14, 17].

A last, but important, remark has to be made here. The tetrahedral bonding model, which determines the number of energy levels inside the band gap, is only valid for impurities located on substitutional sites. Therefore, due to their strong influence on the electrical properties of semiconductors, lattice site location studies of impurities are important [18].

1.2.1.2 Magnetic properties

In dilute magnetic semiconductors (DMS), transition metal dopants are incorporated in otherwise non-magnetic semiconductors to make them ferromagnetic. Exhibiting both semiconducting and ferromagnetic behaviour, dilute magnetic semiconductors are investigated as promising materials for semiconductor spintronics[1]. Although Mn doped III-V semiconductors (e.g. GaAs and InAs) are the most successful dilute magnetic semiconductors, elemental semiconductors (Si and Ge) are also extensively investigated for this purpose [20]. For example, the theoretical modelling of the DMS behaviour benefits from the relatively simple structure of Ge compared to compound semiconductors, such as GaAs and InAs.

In general, the magnetic and electric behaviour of DMS materials is strongly dependent on the lattice location of transition metals. The typical example is Mn doped GaAs,

[1] Spintronics is the area of condensed-matter physics that studies the properties of the electron spin, in order to improve the efficiency of electronic devices and to enrich them with new functionalities [19].

where substitutional Mn provides both the magnetic moment and the free hole that mediates that magnetic interaction, while interstitial Mn acts as a magnetic and electric compensating defect (decreasing both the magnetisation and the ordering temperature) [12]. However, the relation between the lattice sites and the magnetic properties is still poorly understood in Mn doped Ge. Furthermore, the magnetic behaviour of DMS materials, including Mn doped Ge, is strongly dependent on the spatial distribution of the magnetic dopants (dilution versus segregation). For example, the ordering temperature increases with increasing concentration of *dilute* Mn in Ge (i.e. randomly distributed Mn in Ge sites). On the other hand, if the transition metals segregate into a *secondary phase* (e.g. metallic Mn in Ge, or MnAs in GaAs), the material is not considered to be a DMS [20].

1.2.1.3 Diffusivity: diffusion mechanisms

The electrical and magnetic properties of transition metals in Ge depend on their lattice site locations. On the other hand, the diffusion mechanisms of these impurities inside the Ge lattice give interesting information on how dopants have preferences to diffuse through the lattice (e.g. during the thermal annealing).
Diffusion is *the process of migration of atoms through a solid* [2]. Diffusion in thermodynamic equilibrium[2] is described as a thermally activated process. Typically, the diffusion coefficient follows an Arrhenius law:

$$D = D_0 e^{-\frac{E_a}{k_B T}},$$

with the pre-exponential factor or jump frequency factor D_0, the activation energy of the diffusion E_a and the Boltzmann constant k_B.

In general, atoms (either from the host or impurities) may diffuse following different mechanisms. In the interstitial mechanism (see figure 1.3.a) the diffusing atoms are self-interstitials, i.e. Ge atoms that are not located on substitutional positions. Figure 1.3.b shows the vacancy-related mechanism, in which the diffusing atom goes from a substitutional to another substitutional position by jumping into a vacancy. Both mechanisms might be present in the Ge self-diffusion equation:

$$D = D_{0I} e^{-\frac{H_I}{kT}} + D_{0V} e^{-\frac{H_V}{kT}}.$$

[2]When the diffusion time is not large enough at a specific temperature to get an equilibrium density of intrinsic point defects, non-equilibrium diffusion occurs (e.g. transient-enhanced diffusion (TED)).

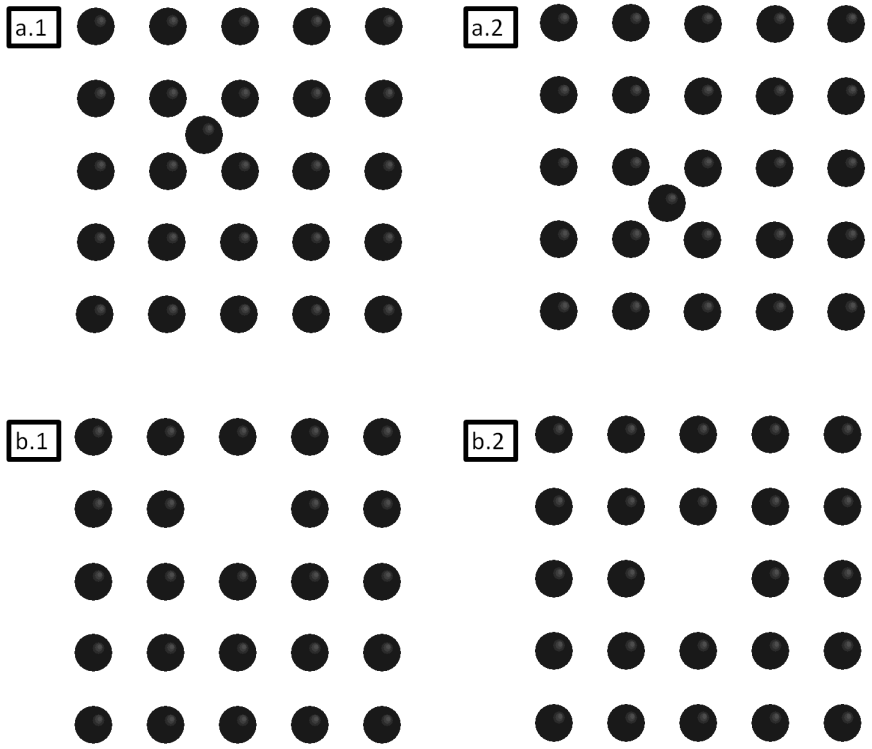

FIGURE 1.3: a. interstitial diffusion mechanism; b. vacancy-mediated diffusion mechanism

However in contrast to Si, only one mechanism seems to be present in Ge [21]. It is generally accepted that the self-diffusion in Ge is vacancy-mediated. One of the clues supporting this statement is the ab initio calculation of the formation energy for a vacancy [22]. This energy is smaller for Ge than for Si. Experimentally, this self-diffusion mechanism for Ge is observed as well. By obtaining the Ni or Cu diffusion profiles in Ge, the vacancy-assisted Ge tracer self-diffusion coefficient is deduced [23]. Also earlier radioactive tracer diffusion measurements reached a similar result [24]. The self-diffusion coefficient of Ge for a temperature range between 535°C and 904°C can be expressed as

$$D_{\mathrm{Ge}} = 13.6\ e^{-\frac{3.09\mathrm{eV}}{kT}}\ \mathrm{cm}^2\mathrm{s}^{-1},$$

which was obtained by Werner *et al.* in 1985 [25].

For Mn impurities in Ge, the literature suggests a diffusion mechanism similar to the Ge self-diffusion [26]. An explanation is given by the closely related diffusion coefficient of Mn in Ge to the one of the Ge self-diffusion. The diffusion coefficient

is obtained by Mn deposition on a Ge substrate using molecular beam epitaxy and is valid in a temperature range from 450°C to 600°C. This technique introduces vacancies, although in principle, a higher vacancy concentration is obtained by using ion implantation. The diffusion coefficient of Mn in Ge is given by

$$D_{\mathrm{Mn}} = 1.72 \cdot 10^{-3}\ e^{-\frac{2.37 \pm 0.01\mathrm{eV}}{kT}}\ \mathrm{cm^2 s^{-1}}.$$

Although this work mainly suggests the occupation of S sites due to a vacancy-mediated process, the diffusion can also be regulated by complex point-defects like Mn-vacancy pairs (see also section 1.3).

At the other extreme, there are impurities in Ge which diffuse through a direct interstitial mechanism. These dopants are the fastest diffusers, because interstitial diffusion is typically faster than vacancy-mediated diffusion. This is due to the weaker bonding of an interstitial atom (compared to a substitutional impurity) with the surrounding atoms. There are also more interstitial positions available than vacancy sites to jump to. An example of an impurity that moves through the Ge lattice using the direct interstitial diffusion is Fe. At a temperature of 800°C, the observed diffusion coefficient for Fe in Ge lies between 10^{-6} and 10^{-7} $\mathrm{cm^2 s^{-1}}$, with an activation energy around 1 eV [27]. In addition, when vacancies are present in the lattice, also impurity-vacancy defects may be present.

Cu and Ni use a different diffusion mechanism. Cu is the textbook example of dissociative diffusion or Frank-Turnbull mechanism [28]. In 1955, Van der Maesen and Brenkman had already proposed a model where the Cu atoms on substitutional positions ($\mathrm{Cu_s}$) are in a temperature dependent equilibrium with the ones on the interstitial sites ($\mathrm{Cu_i}$) [29]. They assumed a different diffusion constant for the interstitial and substitutional atoms. In 1956, Frank and Turnbull made a comprehensive model (see figure 1.4) that emphasises the importance of the presence of vacancies [28]. This dissociative model can be represented as

$$\mathrm{Cu_i} + \mathrm{V} \longleftrightarrow \mathrm{Cu_s}.$$

The rapidly migrating interstitial impurities recombine with a vacancy, whereby a much slower travelling substitutional dopant is created [23]. The reverse and forward process is very fast, therefore, the interstitial-substitutional replacement forms no rate limiting factor in the diffusion process. Experimental research found two different diffusion coefficients for Cu in Ge. Therefore, two diffusion regimes are present: vacancy- and $\mathrm{Cu_i}$-controlled diffusion.

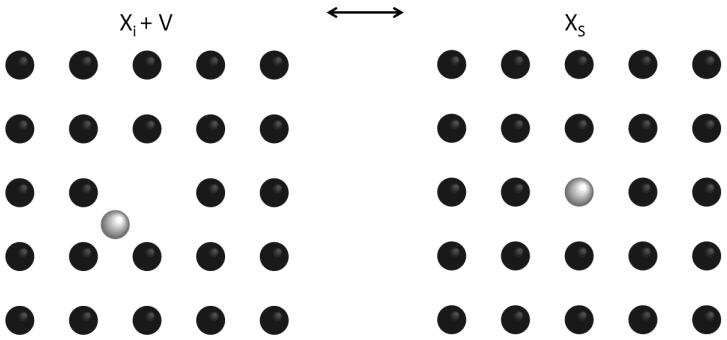

FIGURE 1.4: Frank-Turnbull or dissociative diffusion mechanism. The figure on the left is step number one ($Cu_i + V$) and on the right number two (Cu_s). The steps can take place in reverse order.

Values of diffusion coefficients for Ni or Cu in Ge are found in the literature. For Cu, a vacancy-controlled diffusion coefficient of

$$D_{\mathrm{Cu_V}} = 5.5e^{\frac{-1.55\mathrm{eV}}{kT}}\ \mathrm{cm^2 s^{-1}}$$

and a Cu_i-controlled diffusion coefficient of

$$D_{\mathrm{Cu_i}} = 7.8 \cdot 10^{-4} e^{\frac{-0.084\mathrm{eV}}{kT}}\ \mathrm{cm^2 s^{-1}}$$

were reported by Bracht *et al.* [30].
In 1959, an effective diffusion coefficient of Ni in Ge was described by Tyler, which was given by $5 \cdot 10^{-5}$ $\mathrm{cm^2 s^{-1}}$ at 875°C [14]. However, also Ni in Ge uses the dissociative diffusion mechanism as Cu in Ge. Therefore, in 1997 by the use of the room-temperature spreading-resistance technique, a Ni_i-limited diffusion coefficient of Ni_s about

$$D_{\mathrm{Ni_i}} = 2.0 \cdot 10^{-5}\ \mathrm{cm^2 s^{-1}}$$

and a vacancy-limited diffusion coefficient of Ni_s around

$$D_{\mathrm{Ni_V}} = 1.5 \cdot 10^{-6}\ \mathrm{cm^2 s^{-1}}$$

were found after rapid thermal annealing at a temperature of 800°C [31]. By comparing the diffusion coefficients of Cu_i and Ni_i at 800°C, Ni_i is the slowest of the two in Ge.

1.2.1.4 Solubility

The solubility (S_0) is a measure of the tendency for impurities to remain randomly distributed or to segregate inside the host material. In general, S_0 of an impurity in a solid phase is defined as the maximum concentration of that impurity in thermodynamic equilibrium with the liquid phase of a material [2]. Hall described the temperature dependence of the solubility as follows [32]: S_0 becomes larger while decreasing the temperature, starting from the melting point. At a particular temperature, S_0 reaches a maximum value, after which the solubility lowers again, even when further decreasing the temperature.
For many impurities in germanium, the solid solubility is estimated based on the knowledge of the distribution coefficient (k_d) of the element at the melting point of Ge [33]. This distribution coefficient is the relation between the concentrations of the two immiscible phases [2], or

$$k_d = \frac{C_{solid}}{C_{liquid}}.$$

In 1959, Trumbore published an overview of different distribution coefficients at the melting point of Ge. Values of k_d are of the order of 10^{-6}, $3 \cdot 10^{-5}$, $3 \cdot 10^{-6}$ and $1.5 \cdot 10^{-5}$ for Mn, Fe, Ni and Cu in Ge respectively [33]. In general, transition metals in germanium show a low solid solubility. Therefore, they have a large tendency to cluster. Apart from the available distribution coefficients estimated by Trumbore, some qualitative data are available in the literature. In 1959, it had already been stated that the solubility of Mn in Ge is lower than the one for Ni in Ge [14]. The tendency for Mn to cluster in Ge was reported by Continenza *et al.* [34]. The solubility of Cu in Ge, in turn, is higher compared to the one of Ni in Ge [2].

1.2.2 Lattice site location

In general, when impurities are introduced into a lattice, there are two possible locations. Impurities may occupy a substitutional (S) site, where the impurity replaces a Ge host atom. All other possible sites are interstitial locations. Based on symmetry conditions, some of these sites are more preferred to be occupied than others [36]. In figure 1.5, a number of high symmetry lattice sites in the (100)-plane of a Ge lattice is illustrated.

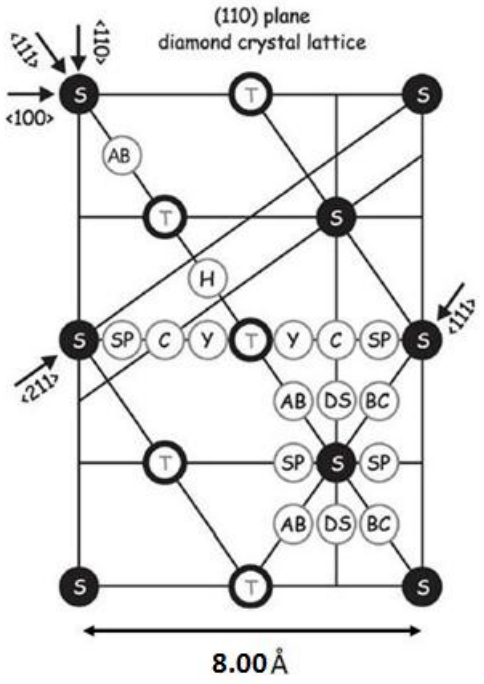

FIGURE 1.5: High symmetry lattice sites in the (100)-plane in Ge lattice [35].

Two high symmetry interstitial sites are important for the results in this thesis. One of them, the bond-centered (BC) site, is located between two nearest neighbouring S sites along the $< 111 >$ direction. Another used high symmetry site is the tetrahedral (T) interstitial site, that has a cubic symmetry.

Some information about the lattice site location of transition metals in Ge is available in the literature. Electrical measurements (Hall and Deep Level Transient Spectroscopy (DLTS)) indicated a preference for the substitutional site [37, 38, 39]. Also ab initio calculations indicate a favoured S site over the T site for 3d transition metals [40]. However, other experiments indicate the possibility for an impurity to be on a non-substitutional site as well. In 2003, an emission channeling experiment, where ^{67}Cu-ions were implanted in Ge, showed a large fraction of the Cu atoms on the S site, but also a smaller amount on a location displaced from an ideal S site [41]. In the same year, emission Mössbauer spectroscopy suggested an occupation of the S site, T site and a position that was related to an impurity-vacancy complex [42]. The T site was assumed to be present due to the recoil upon β-decay of the implanted ^{57}Mn atoms to ^{57m}Fe . The recoil energy (40 eV) is sufficiently high to overcome the barrier from the S site to the T site, but it is nog high enough to reimplant all the ^{57m}Fe impurities [40].

1.3 Ion implantation: production of defects

Semiconductor doping (e.g. introducing impurities into silicon and germanium) may be done by in situ doping, where the host material is doped during growth. However, in this thesis, the transition metals are introduced in Ge by the use of ion implantation, which has a high-throughput. This has its consequences for the vacancy concentration available after doping.

Since ion implantation allows to very accurately control the purity, fluence [3] and depth of the implanted impurities, it has an important application in the current integrated circuit (IC) technology. Therefore, it is important to know what these implantations induce in the investigated materials.

Two types of interactions contribute to the amount of kinetic energy lost by a charged particle passing through a material [43]:

$$\left(\frac{\mathrm{d}E}{\mathrm{d}x}\right)_{\text{total}} = \left(\frac{\mathrm{d}E}{\mathrm{d}x}\right)_{\text{nuclear}} + \left(\frac{\mathrm{d}E}{\mathrm{d}x}\right)_{\text{electronic}}$$

The interaction between the bound or free electrons in the solid with the impinging charged particles forms the electronic part. On the other hand, the nuclear part comes from the interaction between the charge of the incoming particles and the nuclei in the solid. These latter collisions are responsible for the implantation damage in semiconductors.

The amount of damage produced by ion implantation depends on the host lattice in which the impurities are implanted. It appears that for the same implantation temperature, more damage is present in Ge than in Si [44]. In addition, also other damage related parameters are present. First of all, there will be more disorder when the fluence is higher [45], since the amount of displaced Ge atoms may increase. Also a higher ion mass will lead to the same consequence [46]. Another very important parameter is the implantation temperature. It is possible to reduce the amount of disorder during implantation by increasing this temperature. That is why the experiments done in this thesis use an elevated implantation temperature.

Based on the fluence, different regimes can be classified [47]. In the lowest ion fluence regime, the maximum defect fraction and strain are linearly proportional and only small and isolated defects will be present. For a higher fluence, larger defects lead to a less crystalline lattice. At a certain point, the fluence is high enough to produce

[3] The fluence or dose is the total number of implanted impurities per areal unit (in atoms/cm^2).

amorphization. However, for the experiments in this thesis, all used fluences are below this threshold.

1.3.1 Native defects

When the energy transfer from the incoming ion is larger than the displacement threshold energy, ion implantation can induce different types of defects. A point defect is obtained when the periodicity of a lattice is changed in a single point. There are different types of point defects (see figure 1.6). If a lattice site is empty, the defect is called a vacancy (V). A self-interstitial (Ge_I) is obtained when the displaced target atom does not reside in a substitutional position. When a self-interstitial and a vacancy are combined, a Frenkel pair (Ge_I - V) is obtained [48].

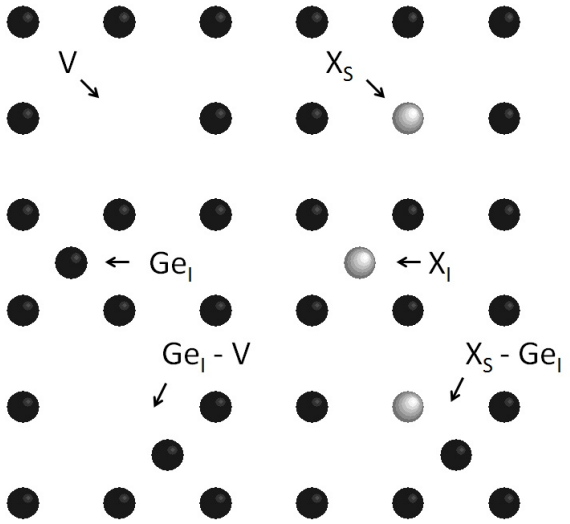

FIGURE 1.6: Example of point defects. An open space is called a vacancy (V), the black circles are Ge atoms and the grey circles are impurities. Other point defects are a self-interstitial (Ge_I), a substitutional (X_S) and an interstitial (I_I) impurity. Also an impurity-vacancy (X_I - V) and an impurity-self-interstitial (X_S - Ge_I) complex are visible.

Other types of defects are line and planar defects. Examples of line defects are edge and screw dislocations. A last type of imperfection is based on defects in three-dimensional clusters, called volume defects. Typical examples are cluster vacancies, called voids. Apart from defects only related to Ge atoms, defects that incorporate impurities are also possible.

1.3.2 Impurity-related defects

Besides native defects, ion implantation also creates combined defects related to the implanted impurities. In figure 1.6, different point defects are illustrated. When the impurity atom is positioned on the site of a host atom, a substitutional impurity (X_S) is obtained. This is in contrast to an interstitial impurity (X_I), which occupies a site in between the host atoms. A (substitutional) impurity and a self-interstitial complex (X_S - Ge_I) is obtained when a self-interstitial is present next to an impurity atom. Analogously, a complex composed of an interstitial impurity and a vacancy (X_I - V) can be created. For this latter type of complexes, Höfler *et al.* theoretically illustrated the formation of distorted substitutional complexes for impurities of the 3sp (e.g. aluminium (Al)) and 4sp (e.g. arsenic (As)) series [49]. For dopants of the 5sp (e.g. antimony (Sb)) and 6sp (e.g. bismuth (Bi)) series, the so-called split-vacancy configuration is preferred. This configuration is related to the BC site in Si and Ge. For transition metals in Ge, this impurity-vacancy complex was also found [40].
In general, many different configurations of the impurity-vacancy complex are possible. However, this thesis focusses on two different types. In the full-vacancy configuration (see figure 1.7.a), dopant A stays on the substitutional position with a vacancy as nearest neighbour. On the other hand, the split-vacancy configuration (see figure 1.7.b) puts the impurity B on the BC location, which is surrounded by two nearest neighbouring vacancies.

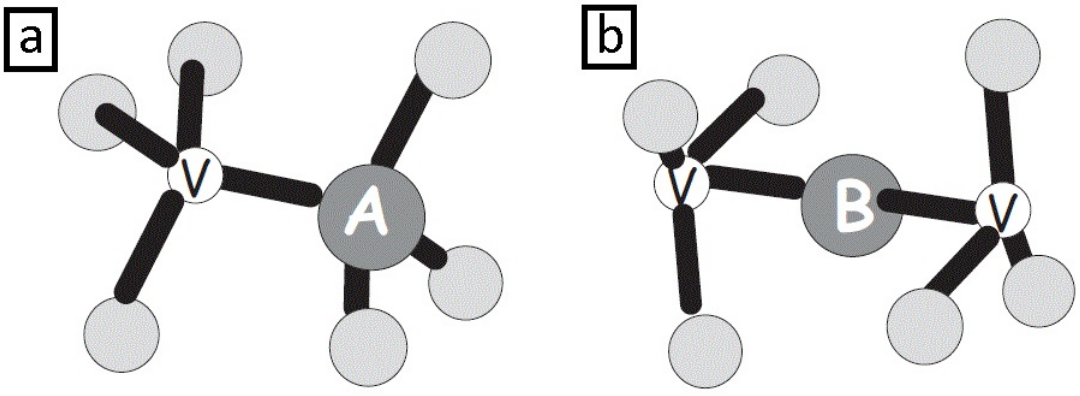

FIGURE 1.7: a. full-vacancy configuration (V is the vacancy, A is the impurity). b. split-vacancy configuration (V are the vacancies, B is the impurity) [17].

Which one of the two configurations is preferred, depends on the heat of formation to occupy these complexes [40]. The heats of formation have been calculated by the augmented plane wave and local orbitals method within density functional theory (as implemented in the WIEN2K code [50, 51]). The heats of formation (ΔH) to occupy a S, T, split-vacancy (or BC) or full-vacancy (or S+V) configuration for Cu, Fe and Mn impurities in Ge are shown in table 1.1.

ΔH (eV)	S site	T site	split-vacancy configuration (or BC)	full-vacancy (or S+V)	references
Fe	1.90	3.19	3.85	4.13	[40]
Cu	1.34	1.75	3.10	3.57	[40]
Mn	2.28	not determined	4.05	4.51	[52]

TABLE 1.1: Heat of formation for different possible occupied sites and configurations for some impurities in Ge.

From table 1.1, it is clear that the occupation of the S site is the most favourable one. This preference for the substitutional site over interstitial sites is also related to the lower vacancy formation energy in Ge compared to Si [26]. The split-vacancy configuration is spontaneously formed, because the heat of formation to occupy the BC site is smaller than the one for the full-vacancy configuration. The latter is the sum of the heat of formation to occupy a substitutional site and the one for creating a single vacancy in Ge (2.23 eV [22]). Therefore, by trapping one of the mobile vacancies present in the Ge lattice after ion implantation by an impurity on the S position [53], the implanted ion will spontaneously evolves into the BC site. It is also possible to have even more complex structures for which it is likely to occupy another high symmetry lattice site. Although, some investigations have already been performed, these larger defect complexes are not yet completely understood.

1.4 Goals

The goal of this thesis is to investigate the implantation of impurities in Ge. In a broader context, and on the long run, studying another host material than Si can be of interest to obtain favourable characteristics (e.g. higher speed) for microelectronic applications. In particular, the *lattice site location of Mn and Ni in Ge* are determined. These studies make an estimate of the *fraction* of the total impurities on a particular lattice site. Moreover, the *thermal stability* is determined, which represents how these fractions vary as a function of annealing temperature.
Finally, the investigations of Mn and Ni in Ge will be compared to other, previously investigated 3d transition metals, with the aim to deduce general trends and differences of the lattice sites of implanted transition metals in germanium.

Chapter 2

Electron emission channeling

In order to determine the lattice sites of impurities in Ge, electron emission channeling was used. First of all, radioactive ions are implanted in a lattice. These ions decay, and the decay particles (electrons, in the case of the isotopes used here) will be *channeled* along atomic rows. By using of a 2D position- and energy sensitive detector, a 2D emission pattern is obtained. From these patterns, it is possible to specify the lattice sites of the emitting atoms. This process of electron emission channeling is illustrated in figure 2.1. The different steps will be highlighted in this chapter.

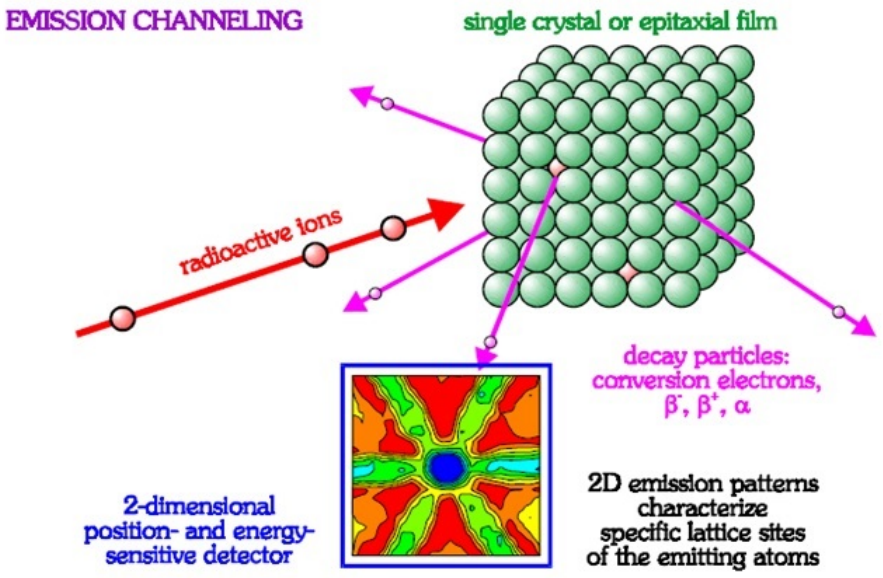

FIGURE 2.1: The principle of electron emission channeling [54].

The electron emission channeling technique is applied in ISOLDE (CERN). This research facility allows to implant radioactive isotopes while simultaneously measuring the electron emission channeling angular anisotropic patterns. This procedure is very important for the analysis of short lived isotopes. After doing such an experiment in CERN, a least square fit is used to compare the experimental patterns to a combination of the simulated ones.

2.1 Electron emission

Electron emission channeling makes use of the charged particles emitted from implanted radioactive ions. In this thesis, the emitted charged particles are β-particles (electrons):

$$^{A}_{Z}X_{N} \rightarrow ^{A}_{Z+1}Y_{N-1} + e^{-} + \bar{\nu}.$$

The energy of the emitted electron continuously varies from zero to the endpoint energy, because β decay is a three body process.
In order to investigate the occupied lattice sites of the implanted ions, radioactive isotopes are implanted in *intrinsic* $< 111 >$ Ge [55]. Information on Mn is given by the electrons originating from the β^{-} decay of ^{56}Mn (2.6h) to ^{56}Fe. For Ni, ^{65}Ni (2.5h) decays into stable ^{65}Cu by emitting β^{-} particles. In analogy, the lattice site location of Cu can be investigated by using ^{67}Cu (61.9h), which emits an electron upon decay to ^{67}Zn. For Fe, ^{59}Mn (4.6s) is implanted in the Ge lattice, which decays into ^{59}Fe. This radioactive isotope of Fe decays with a long half life of 44.6 days into stable ^{59}Co. The lattice site location of the ^{59}Fe nucleus is not influenced by the position of the ^{59}Mn due to an average recoil energy of 200 eV, which is well above the threshold displacement energy of 15 eV in Ge [2], and therefore allows the ^{59}Fe daughter to be reimplanted upon decay.

2.2 Electron channeling

The word channeling or *kanalisierung* was first used by W.H. Bragg in 1910 [56]. His interpretation of what is called X-ray diffraction nowadays, was related to the channeling of X-ray particles through open spaces in the crystal. When L. de Broglie established the wave nature of particles in 1924, X-ray diffraction was thought to be an interference

effect. That is why, it took a long time before the idea of channeling was used again. The concept that the motion of charged particles in a crystal is best described by classical Newtonian mechanics, instead of using wave mechanics, is a key element in channeling.

In general, channeling [1] is the *influence of the crystal lattice on the trajectories of charged particles travelling through the lattice*. The atomic rows and planes of the crystal act as a guide for the ions inside open spaces between rows of atoms. This makes it possible for a beam to enter a crystal and channel along the atomic rows. Conversely, a source of charged particles inside the lattice (i.e. a decaying radioactive isotope) leads to channeling of these species leaving the sample. There exists a reciprocity principle to relate these two trajectories (inward and outward). However, this reversibility of the particle trajectories is only valid when the deceleration caused by scattering of the electrons can be neglected. Therefore, the reciprocity principle can only be applied when radioactive ions are not positioned too deep under the surface.

In order for the electrons to be steered along atomic rows, some conditions are imposed. First of all, the influence on the orientation of the crystal is shown in figure 2.2. Depending on the channeling direction, all electrons will be blocked (see figure 2.2.a) or can be guided through the gap between rows of lattice atoms (see figure 2.2.b).

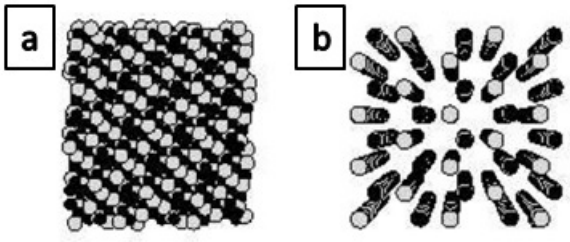

FIGURE 2.2: The amount of channeled electrons that reaches the outside of the crystal depends on the orientation of the crystal [54]. A random direction is shown in the left figure. On the right, a cubic lattice is projected parallel to a crystallographic axis.

The stability requirement must also be taken into account. The negatively charged particles may not deviate too far from the atomic row, because otherwise the steering effect of many collisions is replaced by a wide angle deflection. In this way, a condition must be imposed on the initial direction of the negatively charged particle. Therefore, a Lindhard critical angle exists, which is equal to the maximum angle between the initial momentum and the direction of an atomic row for which a clear channeling effect is

[1] In the concept of emission channeling, axial channeling is used. Planar channeling also exists, but is not highlighted in this thesis. [57]

visible [58]. In contrast, when the channeled particles approach too close to the nuclei of the atom rows, they undergo large angle Rutherford scattering [57].
Another requirement for the electrons is to be able to channel along the row of nuclei. This is based on the fact that the trajectories of charged particles in a solid are determined by Coulomb interactions between those particles and the nuclei. Because channeling a particle evolves many collision, the guided particle interacts with the row of lattice nuclei by interacting with what can be approximated by a continuum potential. This Coulomb force leads to an attraction between the negatively charged electrons and the positive potential of the nuclei in the crystal. Therefore, when an implanted ion occupies a substitutional lattice site, the emitted electrons are steered along the rows of Ge atoms (see upper part of figure 2.3). This substitutional impurity leads to a peak in the electron yield profiles as a function of the emission angle towards the crystal axis. On the other hand, the electrons emitted from interstitial impurities experience a blocking effect. This results in a dip in the electron yield (see lower part in figure 2.3).

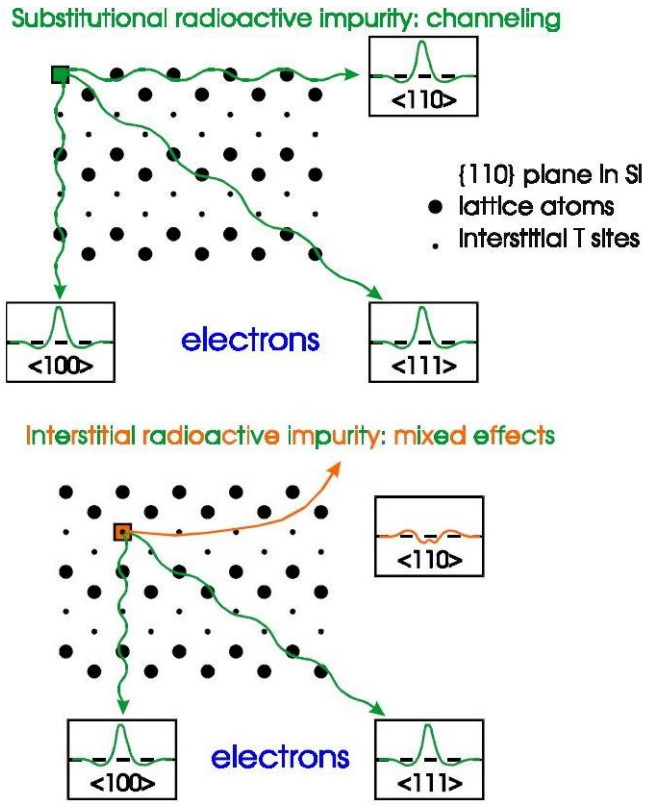

FIGURE 2.3: Electron emission yields along different channeling directions for substitutional (see upper part) and interstitial (see part below) radioactive impurities in a Si lattice (which has the same structure as Ge) [54].

In this thesis, the outcoming electrons are detected along the following four low-index crystal directions: $< 100 >$, $< 111 >$, $< 110 >$ and $< 211 >$. By combining the results along these directions, it is possible to unambiguously identify the lattice sites of the implanted ions.

Note that, the incoherent scattering of electrons, called *dechanneling* [59], has not yet been described. The simulations include electronic scattering by atomic electrons, but also thermal incoherent scattering, coming from vibrating lattice atoms. Although scattering by defects is also a contribution of dechanneling, which is generated by the broken periodicity of the lattice structure, this is not included in the simulations. In general, dechanneling increases with depth.

In conclusion, emission channeling experiments give information about the lattice site location of a radioactive ion implanted in the Ge lattice. Apart from the technique highlighted before, other lattice location techniques could be used. One example is RBS/C (Rutherford backscattering and channeling spectrometry), where the number of *backscattered* ions is measured. Advantages of the emission channeling technique are present compared to RBS/C [60]. First of all, in an emission channeling experiment, a higher sensitivity is achieved down to 10^{12} atoms/cm^2. This is due to the use of radioactive probes, for which less amount is needed compared to the required probe atoms in ion beam channeling methods. Therefore, the emission channeling technique is highly applicable for the investigation of dilute systems. Another advantage is the possibility to investigate impurities with a lighter mass compared to the atoms from the host material. The latter property is important for the lattice location determination of 3d transition metals in Ge.

2.3 Experimental set-up

By using the physics principles of electron emission channeling described in section 2.2, the lattice site locations of Mn and Ni in Ge were determined. Also, the thermal stability of these impurities in Ge was investigated. The implemented technique in ISOLDE (CERN) is described in this section.

2.3.1 Ion implantation: ISOLDE in CERN

The starting point of ISOLDE (On-Line Isotope Mass Separator) in CERN is the PSB (Proton Synchrotron Booster) [61]. From here, a proton beam of 1.4 GeV and intensity up to 2 μA radiates a thick target. Radioactive nuclides can be produced by different processes. In target fragmentation (see figure 2.4 in the middle), a heavy target like ^{236}U is bombarded with the high-energy proton beam, after which the heavy target is fragmented into different smaller species. In the upper part of figure 2.4 spallation is shown. This is a process where small fragments are expelled due to the impact of stress. Fission is also possible when a primary beam with high power hits a well-cooled neutron production target.

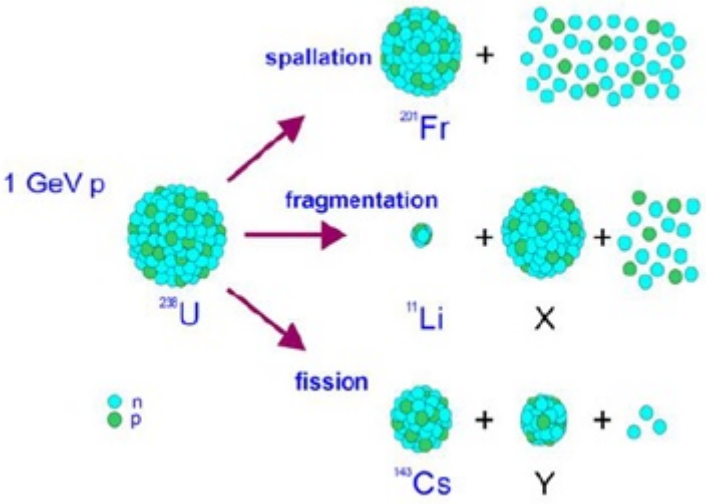

FIGURE 2.4: Possible nuclear reactions to create radioactive ions: fission, spallation and fragmentation [61].

After the production, the isotopes are ionized. In this way, the ionized radionuclides are steered using electromagnetic interactions. The ionization of atoms is obtained by bouncing from a high-temperature metallic surface, which is called a surface ion source [59]. A disadvantage of this type of ion source is the lack of chemical selectivity. To overcome this problem, a resonant laser ion source is used. In this case, the radionuclides are ionized through the stepwise excitation of two or three atomic transitions. This excitation is obtained by lasers, which are very precisely tuned to the energies of the atomic transitions. This type of ion source leads to chemical selectivity, because the energy of an atomic transition is specific for an element. After that, they are extracted and accelerated in a DC electric field created by a high-voltage potential difference

between the ion source and an extraction electrode of the beamline. The next step is the mass separator. There are two types: GPS (General Purpose Separator) and HRS (High Resolution Separator). Both are based on bending magnets, for which the deflection from the beam depends on the mass of the ions. Finally, the beam of radioactive isotopes is transported through a beamline towards the desired set-up.

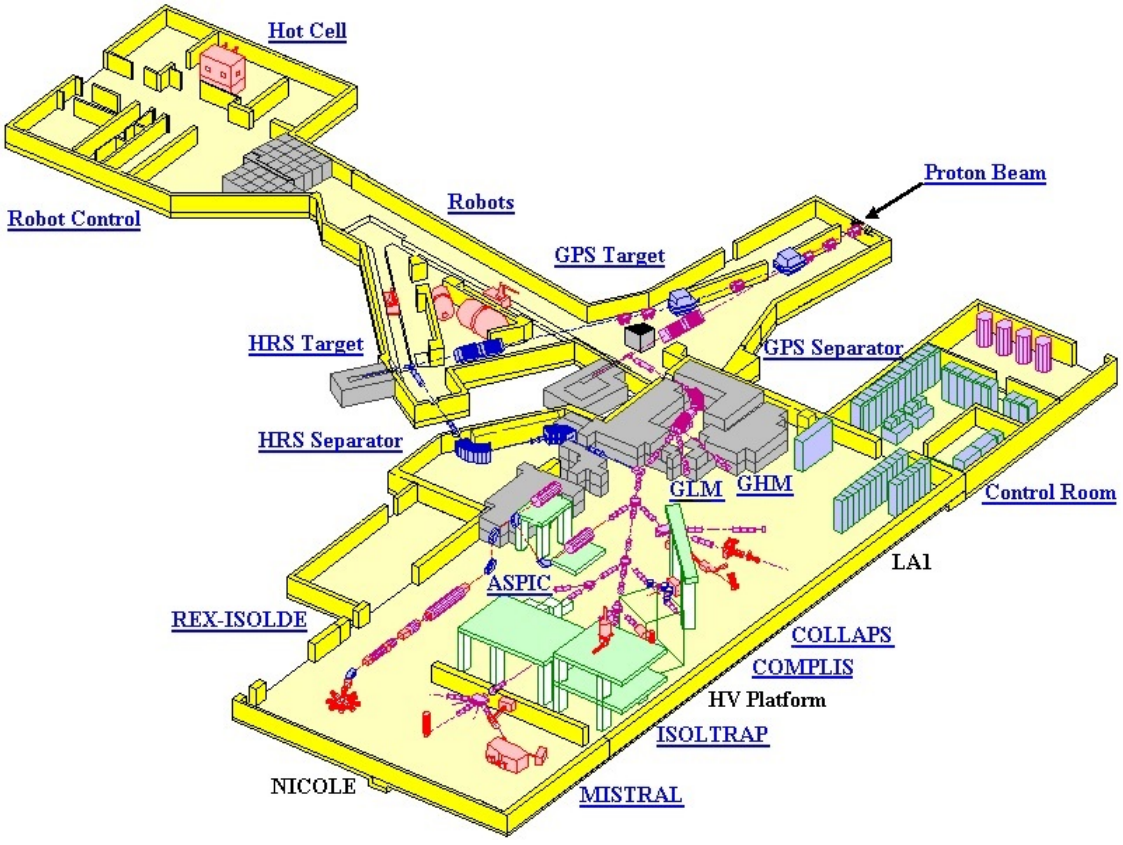

FIGURE 2.5: General overview of the ISOLDE complex [62]. The working principle is given in the text.

2.3.2 Electron emission channeling set-up

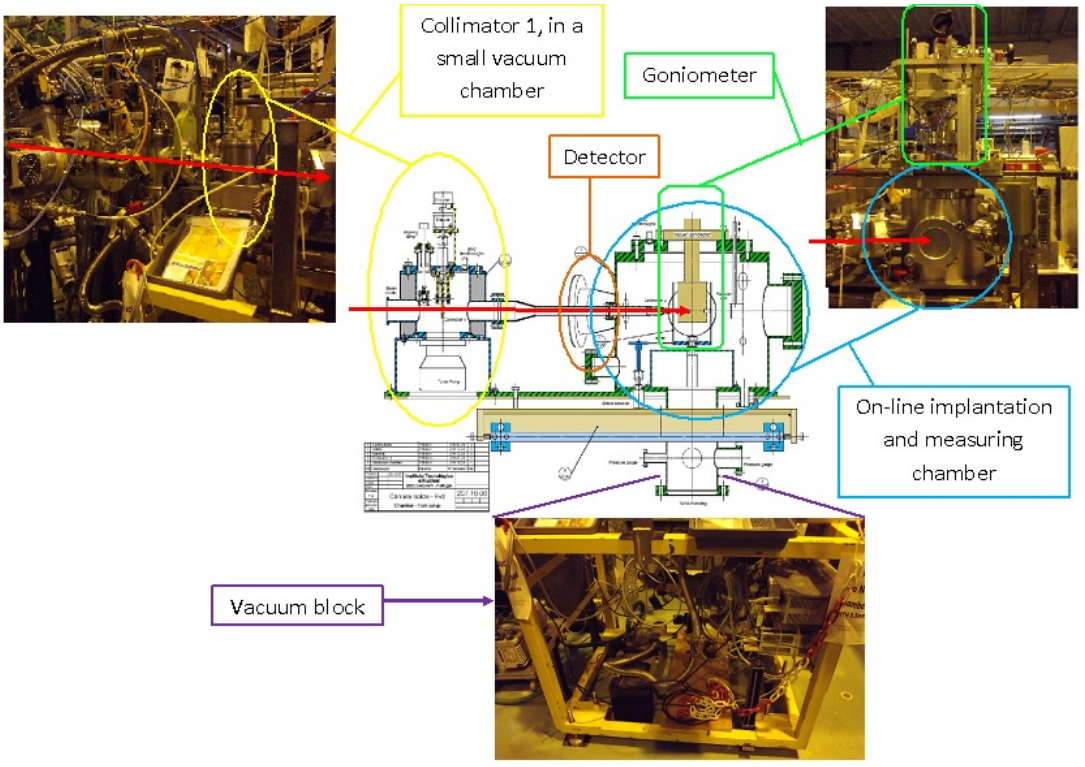

FIGURE 2.6: Schematic side view of the emission channeling set-up. One of the two collimators is shown in yellow [18]. Other important parts of the set-up are highlighted: the detetor (orange), the goniometer (green), the on-line implantation and measuring chamber (blue) and the vacuum block (purple). The direction of the radioactive ion beam is marked in red.

The general emission channeling set-up is shown in figure 2.6. The ions coming from the ISOLDE beamline were implanted in intrinsic Ge, which was mounted inside the *on-line implantation and measuring chamber*. Before the radioactive ions enter the chamber, they pass through two *collimators* (see figure 2.7), which guarantee proper beam positioning on the sample, and defines a circular implantation spot of 1 mm diameter. Shielding is carefully applied in order to minimize the background in the collimators and other set-up parts, originating from the radioactive ions that were implanted.

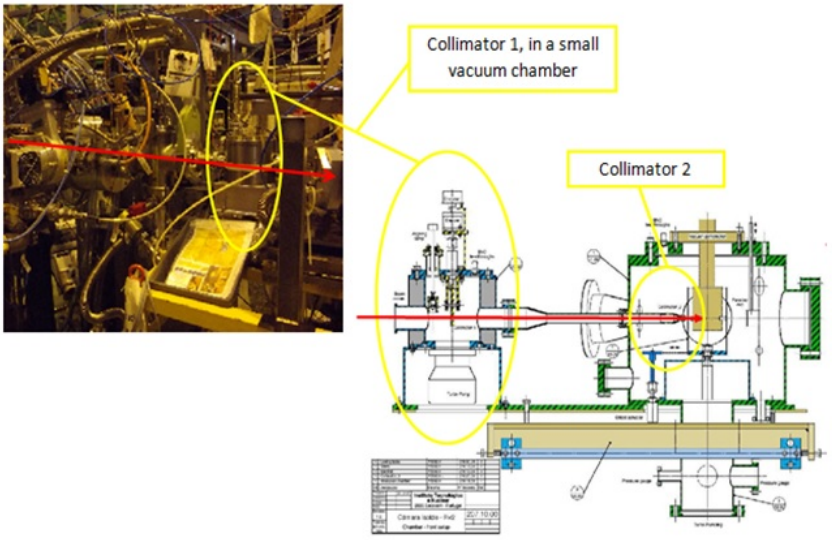

FIGURE 2.7: Schematic side view of the emission channeling set-up. The two collimators are shown in yellow [18]. The direction of the radioactive ion beam is marked in red.

After the collimators, the beam enters the implantation and measuring chamber where it finally reaches the sample. The intrinsic Ge is mounted on a *goniometer*. The experiments shown in this thesis use a 2-axis goniometer (see figure 2.8). Thereby, the sample can be translated in three directions (x, y, z) and rotated around two rotation axes. As shown in figure 2.8, $M1$ rotates the samples around the z-axis and $M2$ rotates the sample azimuthally around an axis perpendicular to the sample-plane.

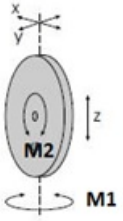

FIGURE 2.8: The 2-axis goniometer used of experiments done in this thesis. $M1$ is the angle for rotating around the z-axis and $M2$ shows the rotation around an axis perpendicular to the sample [59].

The goniometer is equipped with an *in-situ sample heating system*. Hence, resistive warming of the sample up to 900°C is possible. This heating is implemented in order to perform the annealing. Therefore, the thermal stability of the implanted impurities on their particular lattice sites can be investigated. During the annealing, the detector is protected by a thermal shield in front of it. Besides heating up the sample, a closed

cycle helium refrigerator can be used for cooling it down to 50K as well, but this part of the set-up is not used in this thesis.

After the implantation of the ions in the Ge sample, electrons are emitted upon the decay of the radioactive impurities. Conventionally, channeling experiments used a particle detector, which detects one angle at a time [54]. However, the detection efficiency is highly increased when a *position sensitive detector* is used. This type of detector detects the whole solid angle at the same time. It is mounted on the sample chamber under an angle of 17° and at a distance d of approximately 30 cm from the sample (see figure 2.9) [18].

The angular resolution $\sigma(\theta)$ of the technique is determined by the detector, since each pixel has a finite size (σ_d), and by the limited dimension of the implantation spot (σ_b). Therefore, the angular resolution may be defined as follows [59]:

$$\sigma(\theta) \approx \arctan \frac{\sqrt{\sigma_d^2 + \sigma_b^2}}{d} \approx \frac{\sqrt{\sigma_d^2 + \sigma_b^2}}{d} \approx 0.1°.$$

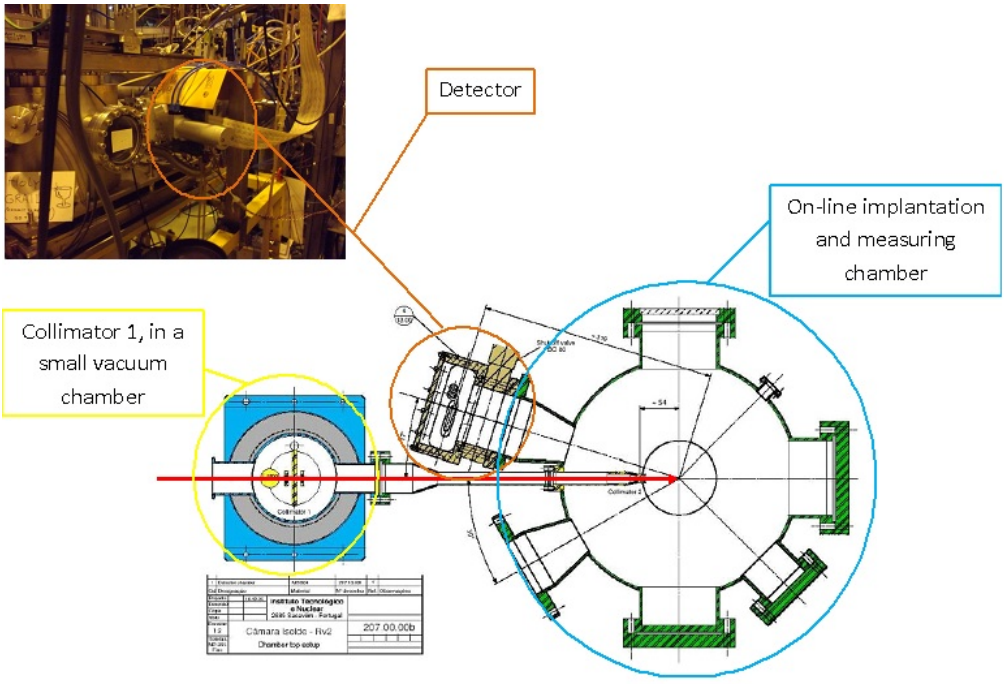

FIGURE 2.9: Schematic top view of the emission channeling set-up. The position sensitive detector is shown in orange [18]. The picture of the detector is a side view. Also the collimator in the small vacuum chamber (yellow) and the on-line implantation measuring chamber (blue) are illustrated. The direction of the radioactive ion beam is marked in red.

In general, the working principle of these types of Si detectors is based on the creation of electron-hole pairs along the particle track [9]. These electrons and holes are separated

by an electric field in the device after which they are collected at the electrodes. The measured signal is proportional to the initial ionization. In the reversed bias configuration, the depletion region (i.e. the region in which there is a suppression of the hole and electron concentration) has the largest size. Therefore, the detector conducts current in this configuration.

In more detail, the detector used in the electron emission channeling set-up is a passivated planar detector. The sensitive area has a dimension of 30.8 x 30.8 mm^2. It consists of 484 pads (or pixels) with a size of 1.4 x 1.4 mm^2 each. The detector is made by a combination of lithography or printing and ion implantation. The position sensitivity is achieved by the connection of the pixels to aluminium contacts, which are connected to a readout system.

In previous implementations in ISOLDE (CERN), the detector was triggered when an electron signal was detected at the backplane of the detector. The off-line set-ups are still equipped with this readout system, since it is sufficient for long-lived isotopes. In this configuration, all the 22x22 pixels are read out sequentially. Afterwards, the analysis of the collected charge is done in each amplifier channel in order to identify the pixel that received the electron. This technique uses very simple and inexpensive pre-amplifier chips, but on the other hand, it is very slow because it reads out each pixel every time. These limitations were eliminated by a new readout system, self-triggering, which only reads out the channels with a trigger. In this way, the rate of the data-taking is increased up to thousands of events per second. This rate is required for on-line experiments with short-lived isotopes. Another disadvantage of the first readout system is the high noise level of the common backplane, because it is subject to the leakage current of the whole detector. With the self-triggering readout technique, however, the trigger signal is generated internally. So the readout no longer suffers from the relatively noisy backplane signal. Because of this, the accessible measurement range of the energy deposited in the detector is increased; the minimum detectable electron energy decreases from 40 keV in the backplane triggering technique, to 25 keV for the self-triggering technique. [18].

Some properties of the detector have to be taken into account in order to get a good detection efficiency. First of all, detector cooling is needed to limit the detector temperature [54], because sometimes the resistive heating system is used. This cooling is done by flowing water around the detector in a pipeline. Secondly, in contrast to X-ray detectors, electron detectors have to operate in vacuum, because a gas atmosphere rapidly spreads and attenuates an electron beam. That is why, the measurements are carried out in vacuum ($< 10^{-5}$ mbar).

Finally, the position sensitive detector measures the electron emission yield. An example of what the detector measures is shown in figure 2.10. The electron yield is represented in a colour plot, where the colour scale defines the height of the electron emission yield.

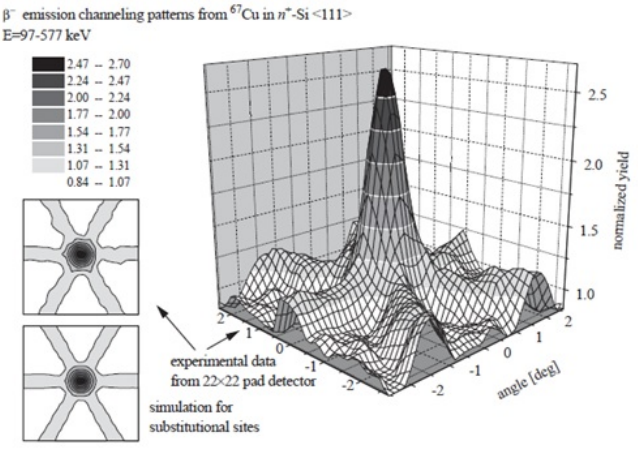

FIGURE 2.10: The experimental data for a β^- emision from ^{67}Cu in n^+-Si $< 111 >$ is shown: the normalized electron emission yield in function of the angle. Under the same conditions, a simulated 2D patterns (left below) is shown for substitutional sites [63].

2.4 Data analysis

2.4.1 Fitting procedure

The experimental patterns from the position sensitive detector are compared to simulated patterns. The simulations are based on the theoretical emission yields calculated by the MANYBEAM software [64]. They are based on the dynamical theory of electron diffraction. The simulations are based on the fact that the electrons have a low mass and energy between 100 keV and several MeV. Therefore, the electrons behave quantum mechanically. The outcome of these simulations are 2D patterns of the electron emission probability $\chi_{\text{theo}(\theta,\phi)}$. These theoretical patterns change for different possible impurity lattice locations. Apart from ideal sites, also locations displaced along a particular direction may be occupied. These displacements are also incorporated in the simulations. In figure 2.11, the influence of the channeling direction on the simulations is shown. The figure also illustrates that some planes show a higher emission yield due to the ordering of the atoms.

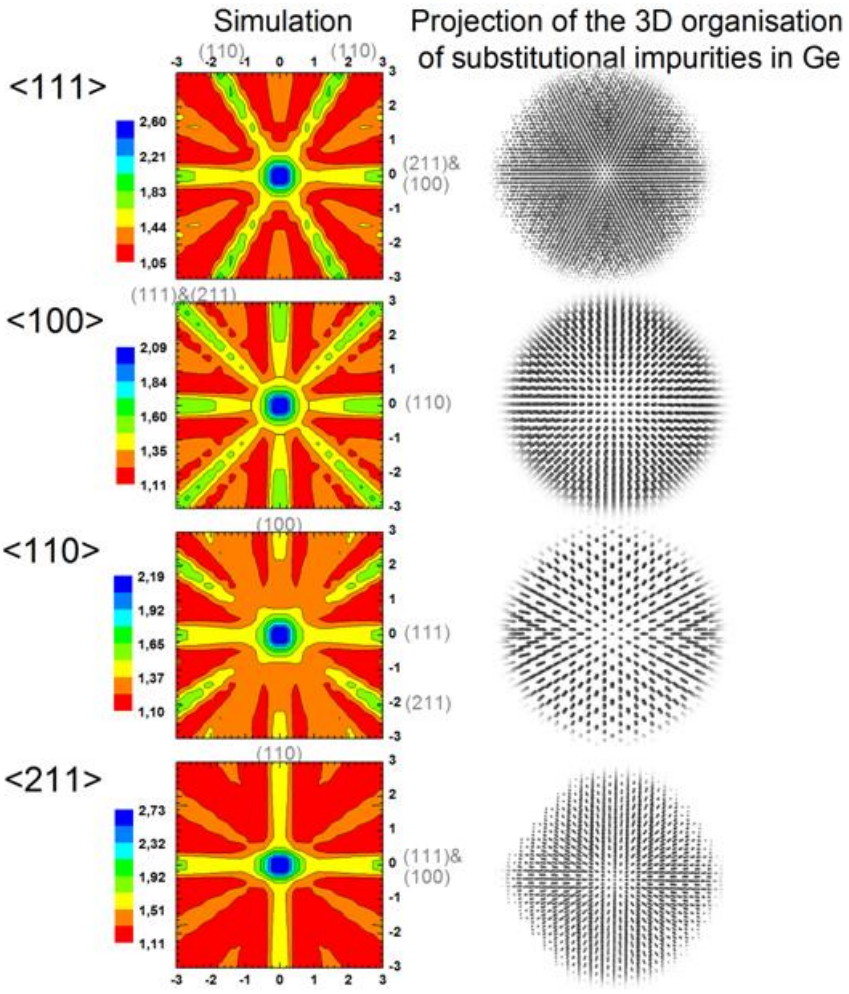

FIGURE 2.11: Comparison between simulated 2D emission channeling patterns of substitutional Mn in Ge and the projection of the 3D organization of atoms on substitutional positions in a Ge lattice (made in CaRIne) along different low-index crystallographic directions. Typically, for substitutional impurities, there is a peak in the middle of the pattern and also a high electron yield along other planes.

The simulations take into account the angular resolution of the technique and the depth distribution of the implanted impurities. Therefore, the SRIM program (Stopping and Range of Ions in Matter [65]) estimates this depth profiles of the implanted transition metals in Ge for a certain implantation energy. Moreover, the root mean square displacement of the crystal atoms u must be specified. For Ge, a typical value is 0.07 Å [54]. Values around this typical value take into account thermal fluctuations, which are isotropic in space. For higher values of u, other effects (i.e. related to defects) may be approximated.

The fitting procedure is done by a least square fit from which a χ^2 is obtaind. In general, this value is defined by [66] (summed over the pixels):

$$\chi^2 = \Sigma \frac{(\text{observed value} - \text{expected value})^2}{\text{expected value}}.$$

In the case of emission channeling, the experimental electron emission probabilities $\chi^{\text{exp}}(\theta, \phi)$ can be expressed in terms of the simulated yields $\chi^{theo}(\theta, \phi)$ [59]:

$$\chi^{\text{exp}}(\theta, \phi) = S(f_1 \chi_1^{\text{theo}}(\theta, \phi) + f_2 \chi_2^{\text{theo}}(\theta, \phi) + f_3 \chi_3^{\text{theo}}(\theta, \phi) + 1 - f_1 - f_2 - f_3).$$

In this formula, S is a scaling factor, which may change in order to obtain a correct normalization. f_1, f_2 and f_3 are the fractions of three different lattice sites where an emitter atom can be localized. The last part of the equation takes into account the random fraction f_R, which equals $1 - f_1 - f_2 - f_3$. This fraction comes from the emitters on sites with low crystal symmetry or from damaged and amorphous surroundings.
The different parameters mentioned before can be simultaneously optimized with the non-linear least square fit. In this way it is possible to determine the fraction of impurities on different lattice sites. Normally, only up to three different sites are investigated in the fit, because when the number of examined sites increases, the sensitivity of the fit decreases. Typically, fitted site fractions below 5% are considered to be below the techniques sensitivity.

2.4.2 Correction factors

The theoretically calculated emission patterns take only into account the electrons that reach the detector without being scattered. These electrons are called direct electrons. However, the electrons may be scattered by parts of the vacuum set-up or even backscatter in the sample (see figure 2.12). These electrons generate a nearly uniform background in the experimental patterns.

The scattered electron background can easily be distinguished in case of a pure conversion electron decay, because conversion electrons have a narrow energy distribution. However, this is not possible for β^- decay, which consists of a continuous energy spectrum over a relatively broad energy window. In order to deduce the total scattering background, the geant4 software is used [67], which includes particle interactions with matter, the geometry of the system and the involved materials.

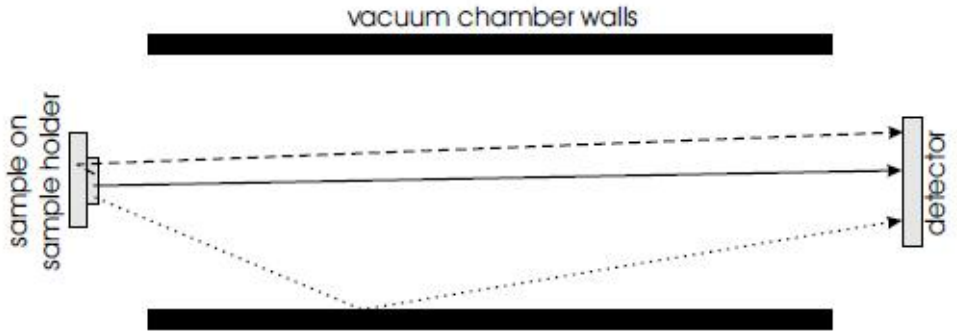

FIGURE 2.12: Possible trajectories in an emission channeling set-up. The solid line represents the direct electrons, the dotted line a possible scattered electron path and the dashed line a backscattered path. [59]

Based on geant4 simulations, it is possible to determine a correction factor which must be calculated for each of the measured crystalline directions. This factor is defined as

$$f = \frac{\text{total electrons}}{\text{total electrons - scattered electrons}} = \frac{\text{total electrons}}{\text{direct electrons}}.$$

For instance, when $f = 2$, for each direct electron, there is one scattered electron that also reaches the detector.

Chapter 3

Experimental results and discussion

The investigated transition metals are manganese and nickel in Ge. For Mn in Ge, three different kinds of experiments will be examined. Apart from an implantation at room temperature, also two experiments at a higher implantation temperature are mentioned. For Ni in Ge, only one experiment at a higher implantation temperature is done which will also show the lattice site locations of the implanted impurities and their thermal stability. In addition, a comparison is made between the 3d-transition metals that have been investigated so far.

Table 3.1 (at the end of this chapter) summarizes some relevant parameters used during the experiment and analysis. Experimental parameters, i.e. isotope, mass, energy, implantation temperature, maximal fluence and tilt angle are listed. The tilt angle (i.e. the angle between the sample normal and the ion beam) is set to 17°, in order to minimize the amount of channeling during ion implantation. This is important because channeling effects are not taken into account in the SRIM simulations (for depth profiles, see section 2.4.1) [65]. Therefore, a random implantation (instead of a channeled one) is used to reliably simulate the depth distribution. In addition, also estimated parameters are described in table 3.1, which are calculated using the SRIM program. First, the depth distribution of the impurities, estimated by SRIM, is used as an input parameter for the MANYBEAM simulations (see section 2.4.1). The mean projected range R_p is the average depth of the implanted impurities. When impurities diffuse towards the surface, higher fitted fractions are obtained. However, a reduced channeling effect is obtained when the impurities are located deeper in the sample compared to the mean projected range. Diffusion lengths of the order of R_p are referred to as *long range diffusions* in this thesis. Apart from R_p, another length

scale is important too. The closest distance between two neighbouring impurities gives an estimation of the length over which impurities have to travel in order to cluster. An estimation of this distance is calculated by using the peak concentration (in atoms/cm^3), estimated using SRIM. Finally, an estimation is made on the number of vacancies produced per ion, which are generated as a result of the ion implantation. Note that this approximation is very rough, because it does not take into account the possibility of defect recombination.

3.1 Manganese in germanium

3.1.1 Experimental details

In order to investigate the thermal stability of the lattice sites of Mn in Ge, ^{56}Mn ($T_{1/2}$ = 2.6 hours) was implanted in a $< 111 >$ Ge lattice, which decays to ^{56}Fe. For this implantation, the fluence was kept below the amorphization threshold of $5 \cdot 10^{12}$ atoms/cm^2 (see also table 3.1). Therefore, the amount of Mn clustering was minimized and a good dilution of the Mn atoms was obtained [52]. The measurements along the $< 111 >$, $< 100 >$, $< 110 >$ and $< 211 >$ directions were performed at room temperature after different annealing steps of 10 minutes up to 600°C in vacuum.

3.1.2 Results

The first experiment evolved an implantation at room temperature. However, the high degree of disorder introduced upon room temperature implantation did not allow adequate data analysis. This is consistent with the well-known low radiation resistance of Ge.

The second experiment was an implantation at 300°C. These measurements clearly indicated the presence of the influence on the fluence. Apart from the experimental patterns measured before annealing, which were already published by Decoster *et al.* in 2010 [52], the measurements after an annealing at a temperature of 400°C had not yet been analyzed. The random fraction increased due to the extra fluence incorporated into the crystal during an extra implantation, which was done in between two measurements after the 400°C annealing.

Finally, an experiment was carried out at a temperature of 250°C, in which the fluence was carefully controlled in order to reduce the amount of damage.

Lattice site location

First, a one-site fit was attempted, whereby the analysis took only one possible high symmetry site into account. This was done for all possible high symmetry sites shown in figure 1.5 as well as for displacements between two high symmetry sites for a smoothing value of $\sigma = 0.1°$. Since inconsistent results were found when comparing the four measured channeling directions, a two-sites fit was tried.

In the two-sites fit, the experimental patterns were compared to the combination of two simulations. Therefore, two different high symmetry lattice sites were allowed. First of all, there was a fraction on a substitutional position. This can be illustrated by looking to the experimental patterns (see figures 3.1 a-d) for which a high electron yield is visible in the middle of the patterns and also along other visible low-index crystal directions, which is typical for Mn_S simulations (see figures 3.1 i-l). In addition, ab initio calculations also showed that the S site is the most favourable one for Mn in Ge (see section 1.3).
By adding the possibility to have a second fraction on the bond-centered position, an improvement in χ^2 of about 10% was obtained compared to the one-site fit. The occupation of the ideal BC site is related to the split-vacancy configuration, which is spontaneously formed when a vacancy is trapped by a substitutional impurity (see also section 1.3.2). When a displacement of about 0.37 Å from the BC site was allowed, an even slightly larger improvement was achieved. Therefore, the possibility exists that the BC-related-Mn atoms all occupied this *near*-BC position. In the literature, the possibility to sit on a displaced high symmetry position is already discussed. For example, in a theoretical calculation of Fe in Si, the potential along the $< 111 >$ direction not always shows a dip on an ideal high symmetry position [68]. Another possible explanation is the partial occupation of Mn atoms on the ideal BC site, which is related to the split-vacancy configuration, and on the near-BC location, which is probably due to a more complex situation with more vacancies involved. Consequently, in general, the occupation of the (near-)BC site is related to the produced defects due to the ion implantation. This two-sites fit gives a fraction of $22 \pm 1\%$ Mn atoms on the S site and $28 \pm 1\%$ Mn on the near-BC location for the as-implanted sample.
By performing the two-sites fit, the two largest fractions had probably already been

found. However, a small improvement of χ^2 (of around 5%) was found compared to the two-sites fit, when also a fraction on the anti-bonding site was allowed. However, the small fitted fraction of $7 \pm 3\%$ on the AB site approaches the sensitivity limit of the technique (see section 2.4.2).

In figure 3.1, a comparison is made between the experimental patterns (a-d) for the four different directions along which the measurements are taken. In the next column (patterns e-h), the best fits of the experimental patterns are shown. These figures are a combination of the simulations of an impurity on the S (patterns i-l) and on the near-BC site (patterns m-p). By comparing the experimental pattern (column 1) to the simulated pattern of Mn_S (column 3), the experimental patterns cannot be reproduced by only allowing the occupation of the substitutional site. This is illustrated by subtracting the Mn_S-simulations from the experimental patterns, which is shown in column 5 (patterns q-t). The experiment-Mn_S column clearly shows similarities to the Mn_{BC}-simulation, therefore supporting the presence of the BC fraction.

Thermal stability

The fitted fractions as a function of annealing temperature are summarized in figure 3.2. In general, the fractions decrease for an increasing annealing temperature. Or, alternatively, the random fraction increases for a higher annealing temperature. Different explanations are possible. First of all, it is possible that Mn atoms are captured by defects, which were introduced by the implantation [69]. In this case, the Mn atoms can occupy low symmetry sites due to the introduced disorder.
It is also worthwhile to consider how far impurities diffuse through the Ge lattice during the annealing of 10 minutes. By using the diffusion coefficient of section 1.2.1.3, which is valid in a temperature range of 450°C to 600°C, the diffusion length ($2\sqrt{Dt}$) after a 10 minute annealing at 500°C is calculated to be around 3 Å. The diffusion length appears to be much smaller than R_p (see table 3.1). Therefore, the increasing random fraction is most likely not due to long range diffusion. Moreover, the estimated diffusion length is also far below the nearest impurity distance. According to this estimation, the Mn atoms are not able to diffuse close enough towards each other during the annealing in order to cluster. However, the diffusion coefficient used in the calculation above is obtained under different experimental conditions compared to the emission channeling experiments. Therefore, the calculation of the diffusion length may not be completely reliable. Furthermore, literature suggests Mn-clustering in Ge: Continenza *et al.* used ab initio calculations to show that a concentration of 6.25% of Mn in Ge leads to the

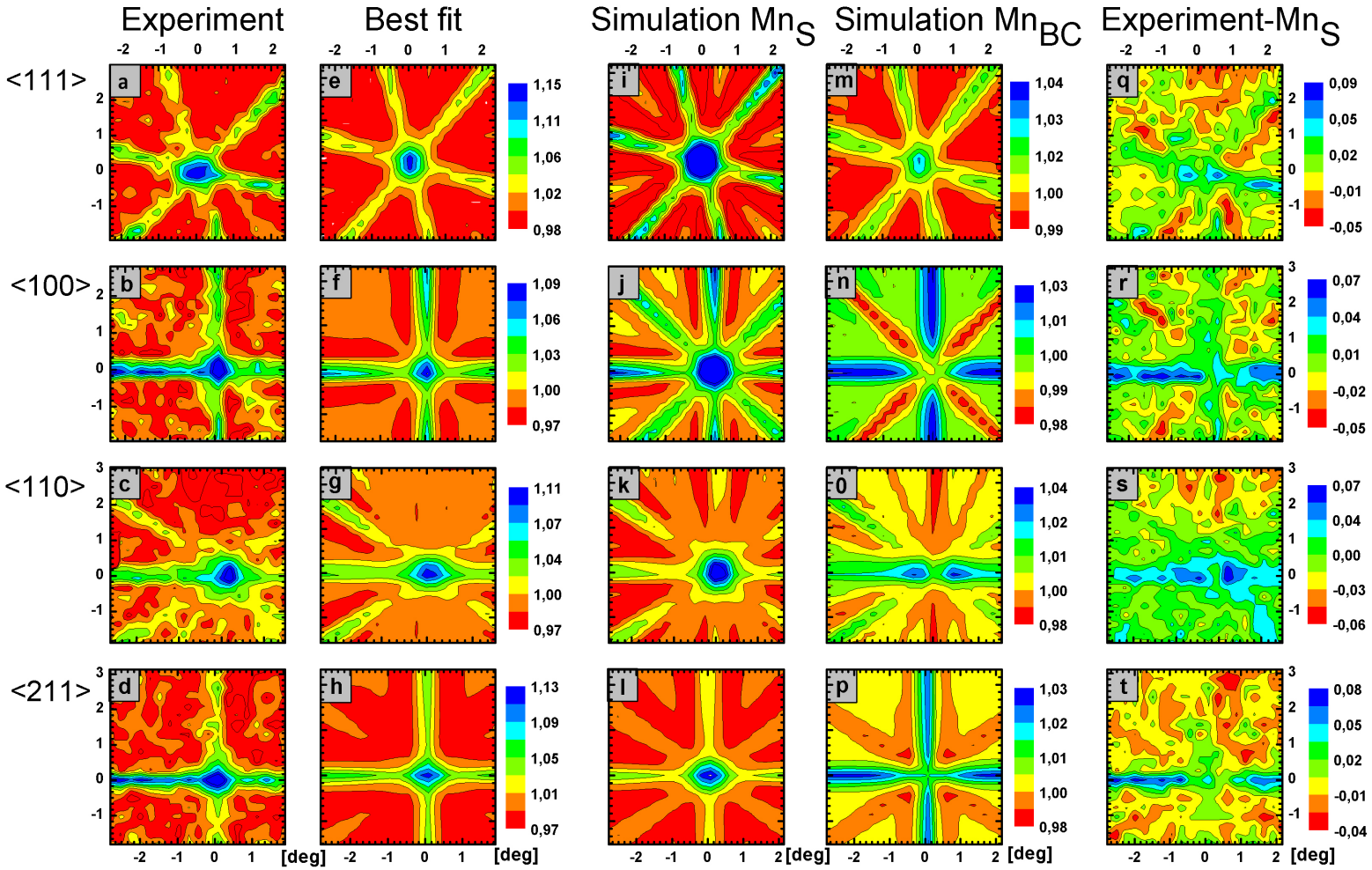

FIGURE 3.1: Comparison over the different directions in order to prove the presence of the BC site (for the measurements on the as-implanted sample). a-d: the experimental patterns; e-h: best fits, coming from the fitting program; i-l: simulated patterns for all the Mn atoms on substitutional positions ($u = 0.07$ Å and $\sigma = 0.1°$); m-p: simulated patterns for all the Mn atoms on near-BC sites ($u = 0.07$ Å and $\sigma = 0.1°$); q-t: difference between the experimental patterns (a-d) and the Mn_{BC}-simulations (m-p).

lowest pairing energy, which is a vital component for the clustering of Mn atoms in Ge [34]. This may be related to the low solid solubility limit of Mn in Ge compared to other investigated transition metals (see section 1.2.1.4).

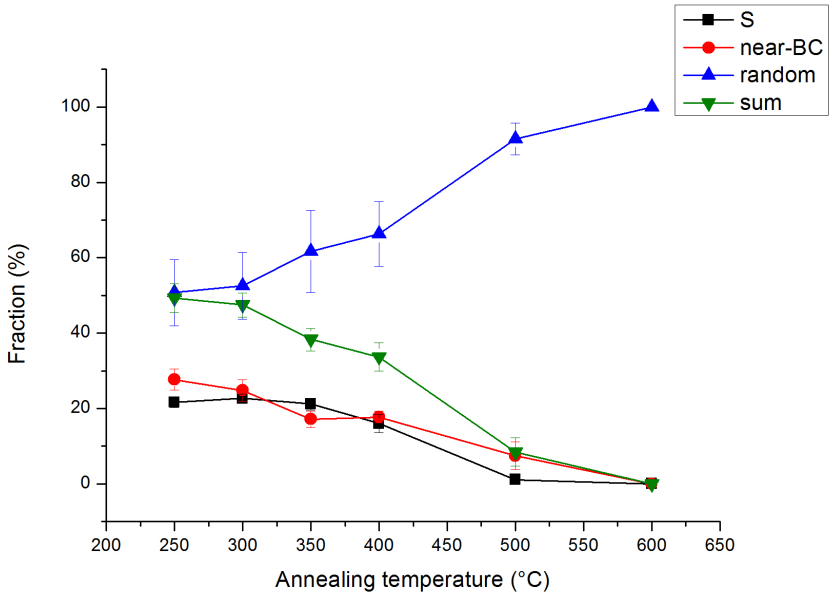

FIGURE 3.2: Fitted fraction as a function of the annealing temperature: the fractions of the different possible lattice sites (S, near-BC, random and the sum (= S + near-BC)) are shown for different annealing temperatures.

From the fitted fraction as a function of the annealing temperature in figure 3.2, the substitutional site is present until 400°C. At an annealing temperature of 500°C, the fraction of Mn atoms on a near-BC position is not yet zero. Finally, after annealing at 600°C, no channeling effect is visible anymore.

From the fitted fractions, an upper limit of the activation energy[1] can be estimated [70]. By using a one-step Arrhenius model, which neglects the possibility of Mn to be retrapped on S sites, an estimation of the activation energy E_a for the dissociation of the substitutional site is calculated as follows

$$E_a = k_B T_n \ln\left(\nu_0 \Delta t \frac{1}{\ln\left(f(T_{n-1}/f(T_n)\right)}\right), \tag{3.1}$$

with T_n the temperature at which the fraction on the S site disappears (500°C), ν_0 the attempt frequency (of the order of 10^{12} s^{-1}), Δt the annealing time (10 minutes) and the fractions at the $(n-1)$th $(16 \pm 2\%)$ and nth (5%) annealing step (obtained

[1]The activation energy is the energy needed to leave an occupied site [70].

from figure 3.2). An estimated E_a of 2.3 eV is calculated, which uses the fact that the lower detection limit of the emission channeling technique is 5%.
It is also possible to take into account an assumption of the number of times an impurity will be retrapped in a particular site before escaping (N) (defined by Wahl *et al.* in [70]). For an energy of 40 keV, this number is given by 526, which uses the rough estimation of the number of vacancies present after the ion implantation (see also table 3.1). In this case, the estimation of the activation energy is given by

$$E_a = k_B T_n \ln\left(\frac{\nu_0 \Delta t}{N} \frac{1}{\ln\left(f(T_{n-1}/f(T_n)\right)}\right), \tag{3.2}$$

which equals 1.9 eV.
On the other hand by using the same procedure, it is possible to obtain an activation energy for the break-up of the BC-related complex. This calculation uses 600°C as temperature at which no fraction on the near-BC site is present any more and $f(T_{n-1})$ equals $7 \pm 4\%$. By using the same formulas 3.1 and 3.2 as for the dissociation of the S site, the upper limit of the activation energy is 2.6 eV, but when the possibility to retrap a Mn atom on the BC site is taken into account, E_a equals 2.2 eV.

The estimations of the activation energy for the dissociation of the substitutional site seem to be lower than the ones for the break-up of the BC-related complex. Therefore, the fractions of the S compared to the near-BC site decrease faster. Although the S site seems to be less stable compared to the near-BC location, the decrease of the fractions on the S and near-BC sites is more or less in the same temperature range (between 400°C and 500°C) (see figure 3.2). Probably, both sites are mobile in this temperature range. First of all, the Mn atoms on the near-BC site may be mobile, because their fraction already decreases at lower annealing temperatures. From the similarity between the activation energy calculated before (between 1.9 eV and 2.3 eV) to the one found in the literature (2.37 eV [26], valid for a temperature range from 450°C to 600°C), the Mn on the S sites may also become mobile in this particular temperature range.

3.1.3 Summary about Mn in Ge

When Mn is implanted in Ge, two major high symmetry lattice sites are occupied. Apart from Mn on substitutional locations, Mn in Ge also occupies near-BC sites. The BC site is related to the split-vacancy configuration, which is spontaneously formed when

a substitutional impurity captures one of the many available vacancies present due to ion implantation.
These lattice sites were determined for different annealing temperatures. The fitted fractions decrease as a function of annealing temperature due to the possibility of defects to migrate during the annealing, which are able to trap Mn atoms. This results in less manganese atoms on high symmetry sites after annealing. From this thermal stability information, the substitutional fraction is present up to 400°C annealing. This is in contrast to the Mn atoms on the near-BC site, which are still present until the 500°C annealing step. However, both sites become mobile in the same temperature range. Finally, after an annealing at 600°C, no channeling effect is observed any more.

3.2 Nickel in germanium

3.2.1 Experimental details

In order to investigate the lattice site locations of Ni in Ge, 30 keV ^{65}Ni ($T_{1/2} = 2.5$h) was implanted in intrinsic $< 111 >$ Ge at a temperature of 250°C. The implantation related parameters of this experiment are shown in table 3.1. The implanted fluence was kept below the amorphization threshold (see section 1.3). The measurements were done at room temperature in vacuum along different directions ($< 111 >$, $< 100 >$, $< 110 >$, $< 211 >$), after annealing at different temperatures (up to 500°C) for a duration of 10 minutes.

3.2.2 Results

Lattice site location

The lattice site locations were determined for very annealing temperature. After trying a one-site fit, where the experimental patterns were compared to one simulation of one particular high symmetry lattice site (σ=0.1°), results along the different measured directions were not consistent. Therefore, a two-sites fit was attempted. Since the experimental patterns showed a peak in the electron yield (see figure 3.3, patterns a and b), one of the two sites is in theory the substitutional position. However, the second site was not clearly distinguishable by looking at the different channeling

directions. Along the $< 100 >$ direction, the second fraction of Ni atoms occupied a near-BC position. However, along all the other directions, a second fraction on a displaced tetrahedral location towards different directions was found. Consequently, the possibility for the Ni atoms to occupy three different high symmetry lattice locations was investigated. This three-sites fit was only possible along the $< 211 >$ and $< 110 >$ directions, because only these two directions are able to distinguish the S from the T site (see also figure 1.5 in section 1.2.2). By going from a two-sites to a three-sites fit, an improvement in χ^2 of around 10% was achieved. For example, in the as-implanted state, the lowest χ^2 was obtained for 15 ± 2% on the S site ($u = 0.065$ Å), 18 ± 1% on the near-BC site ($u = 0.065$ Å and 0.37 Å displaced from the BC site) and 19 ± 3% on the T site, with a root mean square displacement (*rms*) u between 0.22 and 0.40 Å.

It is important to note that the analysis of previous lattice locations experiments in Ge did not include T sites with large rms displacements. Because of the observed inconsistency of the two-sites fit for Ni in Ge, the simulation set was enlarged.

By comparing the experimental patterns from Mn and Ni in Ge along the $< 211 >$ direction (figure 3.1.d and figure 3.3.a), one plane is less visible for Ni compared to the Mn measurement. This already shows a larger probability for Ni atoms to occupy an extra high symmetry site. The presence of the three high symmetry sites for Ni in Ge is also highlighted in figure 3.3. Figures 3.3.a and b show the experimental measurements. The best fits (patterns 3.3.c and d) of these experiments are a combination of the following three simulations: the simulation where the Ni atoms occupy the S site (patterns 3.3.e and f), the near-BC site (patterns 3.3.g and h) and the displaced T site (patterns 3.3.k and l). By subtracting the simulations of Ni_S and Ni_{BC} from the experimental measurement (patterns 3.3.m and n) similarities are present in comparison to the Ni_T simulation. This clearly illustrates the presence of the T site for implanted Ni in Ge.

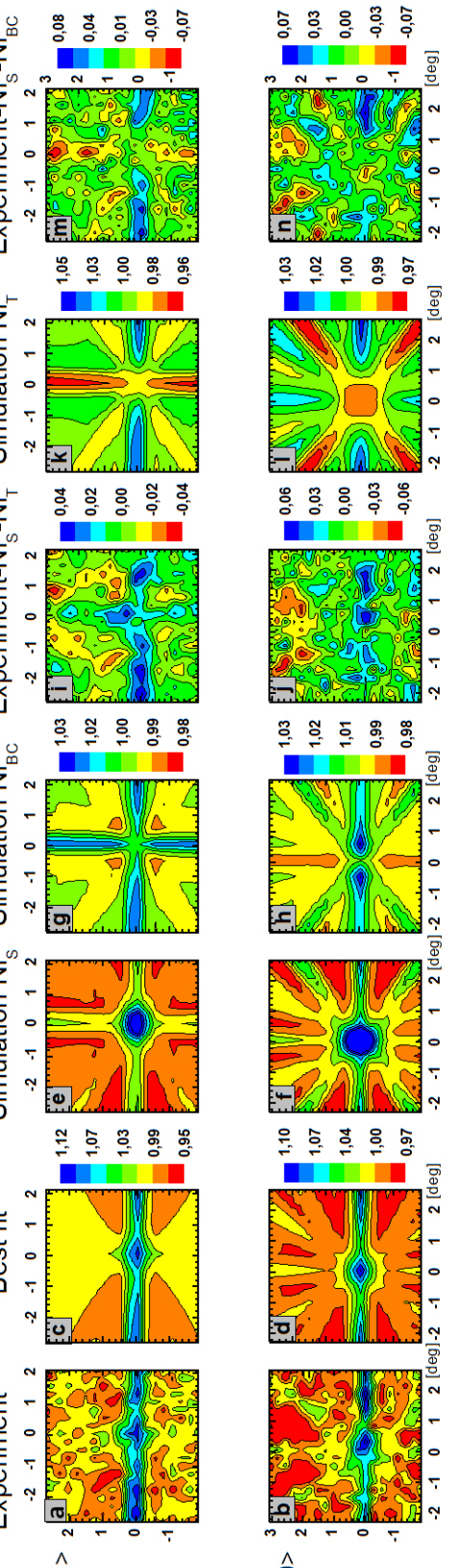

FIGURE 3.3: Comparison over the different directions to show the presence of the BC site and the T site (for the measurements on the sample after the annealing at 350°C). a,b: the experimental patterns; c,d: best fits, coming from the fitting program; e,f: simulated patterns for all the Mn atoms on substitutional positions ($u = 0.065$ Å and $\sigma = 0.1°$); g,h: simulated patterns for all the Mn atoms on near-BC sites ($u = 0.07$ Å and $\sigma = 0.1°$); i,j: difference between the experimental patterns (a,b), the Mn_S-simulations (e,f) and the Mn_T-simulations (k,l); k,l: simulated patterns for all the Mn atoms on T sites ($u = 0.34$ Å and $\sigma = 0.1°$); m,n: difference between the experimental patterns (a,b), the Mn_S-simulations (e,f) and the Mn_{BC}-simulations (g,h).

Thermal stability

The fitted fractions for an annealing temperature up to 500°C are summarized in figure 3.4. Up to an annealing temperature of 350°C, the total sum of the fractions increases or, in other words, the random fraction decreases. This can be explained by the recovery of the implantation damage due to the annealing. Afterwards, the high symmetry fractions decrease. An explanation for this decline can be found in table 3.1. The estimated parameters are compared to the diffusion length of Ni in Ge during an annealing of 10 minutes at e.g. 400°C. An assumption has to be made for the diffusion coefficient of Ni in Ge, because this is not known at a temperature of 400°C. However, the diffusion coefficients of Ni and Cu in Ge are assumed to be of the same order of magnitude (see section 1.2.1.3). Therefore, the diffusion length of Ni in Ge during an annealing of 10 minutes at 400°C is assumed to be of the order of the corresponding diffusion length of Cu in Ge, i.e. 1 μm. Although no literature exists about the clustering of Ni in Ge, this length scale is larger compared to the nearest impurity distance. That is why, clustering is a plausible scenario. The diffusion length is also much larger than R_p. Therefore, the decrease in the random fraction after a temperature of 350°C may be related to inward long range diffusion. Since the depth profile of the implanted Ni-atoms is also an input parameter for the simulations, actually after the annealing, simulations with a larger mean projected range would be required to test this hypothesis. Consequently, the measured and fitted fractions of the implanted Ni are underestimated and have to be considered as lower limits at these higher annealing temperatures. Alternatively, apart from this effect, also other annealing effects may cause an increase in the random fraction. For example, defects have the possibility to migrate due to annealing and are able to trap Ni-atoms in disordered regions. This results in a decreasing sum fraction for an increasing annealing temperature. After the annealing step at a temperature of 500°C, no channeling effect is visible anymore.

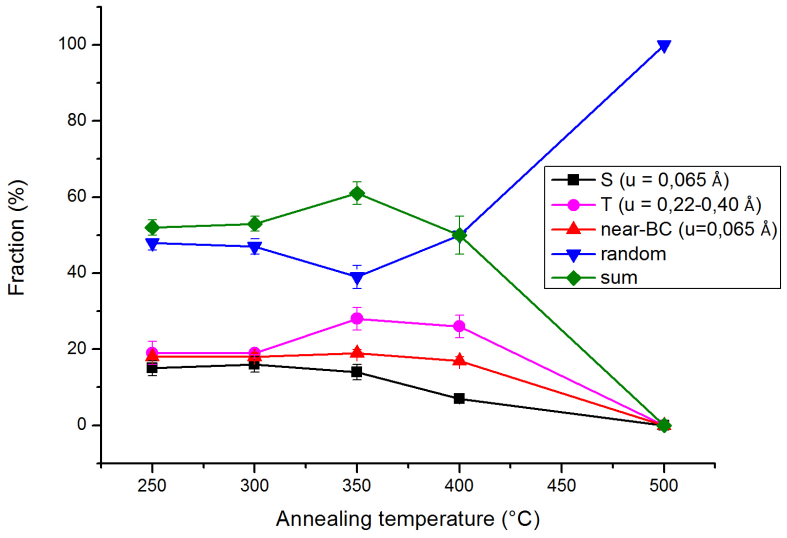

FIGURE 3.4: Fitted fraction as a function of the annealing temperature: the fractions of the different possible lattice sites (S, near-BC, displaced T, random and the sum (= S + (near-BC) + (displaced T)) are shown for different annealing temperatures.

Origin of the T site

The T-site occupation by Ni in Ge is unexpected and had never been observed by any 3d transition metals in Ge. As already highlighted in section 1.3.2, the substitutional site is preferred due to the lowest heat of formation. Moreover, the BC site is related to the split-vacancy configuration (see section 1.3.2). First of all, there is a possibility that a Ni atom on a T site is a free interstitial, where the high u is related to local relaxations [69]. However, there are some suggestions to relate this T site to defect complexes. Therefore, estimations of activation energies are calculated again. The same formulas as in the Mn experiment (formulas 3.1 and 3.2) are used, as well as the assumption of the lower detection limit of 5%. All three sites have disappeared after the annealing of 500°C (see figure 3.4). The number of times an impurity will be retrapped before escaping, is estimated by using the number of produced vacancies due the implantation of 30 keV ^{65}Ni (see table 3.1). Combining the information mentioned before, the activation energy for the dissociation of the substitutional site is estimated to be between 1.94 eV and 2.34 eV[2]. For the break-up of the BC-related complex, E_a lies in between 1.85 eV and 2.25 eV[3]. Also for the break-up of the displaced T

[2]calculations use $T_n = 500°C$, $f(T_n) = 5\%$ and $f(T_{n-1}) = 7 \pm 1\%$
[3]calculations use $T_n = 500°C$, $f(T_n) = 5\%$ and $f(T_{n-1}) = 17 \pm 1\%$

configuration, the activation energy is of the same order, somewhere in between 1.83 eV and 2.23 eV[4]. The estimated activation energy for leaving the displaced T position is rather high compared to the E_a for the free interstitials (see section 1.2.1.3). Typically, free interstitials have a lower activation energy for diffusion compared to substitutional impurities. Since Ni in T sites appear to have a higher activation energy, it is likely that this configuration is associated with defect complexes. Other hints supporting this scenario, are found in the data. First, the fraction of Ni atoms in T sites shows a large rms displacement u. Such a high u compared to the expected value for Ge (0.07 Å) suggests the occupation of a T site in a disordered region instead of an ideal tetrahedral position. Second, the random fraction decreases at the expense of Ni atoms in a displaced T site between an annealing temperature of 300°C and 350°C. In other words, from the 300°C to the 350°C annealing step, disordered regions of the sample are, to some extent, recrystallized. In this recrystallization process, it is plausible that complex defects structures nucleate, in which Ni occupies displaced T sites. These complexes are likely related to more than one vacancy, since, as discussed before, one-vacancy complexes leads, in principle, to the occupation of the BC site.

Although it is likely that the displaced T site is defect related, it remains unclear why until now this particular lattice site has only been observed for Ni and not for other transition metals in Ge. Due to the lack of literature about Ni in Ge, especially under the same conditions as in the emission channeling technique, further studies are required, like for example using X-ray Absorption Fine Structure measurements (XAFS) in order to study the local surroundings of the Ni atoms in T sites.

3.2.3 Summary about Ni in Ge

In summary, three different lattice sites are found for 30 keV ^{65}Ni implanted in intrinsic $< 111 >$ Ge. Apart from the expected substitutional position, also defect related lattice sites are present. A fraction of the implanted Ni atoms resides on the near-BC site, which is related to the split-vacancy configuration. In addition, a fraction of the Ni atoms occupies T sites with a large rms displacement. Arguments were given to relate this displaced T site to defect complexes. All three lattice sites completely disappeared after a 500°C annealing.

[4] calculations use $T_n = 500$°C, $f(T_n) = 5\%$ and $f(T_{n-1}) = 26 \pm 3\%$

3.3 Comparison of different transition metals in Ge

So far, several 3d transition metals have been investigated in Ge by means of the emission channeling technique. The experiments on Fe and Cu in Ge as a function of annealing temperature have been reported by Decoster *et al.* in 2009 [40]. The measurements on Mn in Ge in the as-implanted state have also been reported by Decoster *et al.* [52]. These studies are now extended with the experiments on Mn and Ni in Ge as a function of annealing temperature (see figure 3.6). The implantation related parameters are shown in table 3.2 (at the end of this chapter). Decay properties are highlighted in section 2.1. The maximal fluences are in all cases below the amorphization threshold [17].

In figure 3.5, the fitted fractions on a particular site are compared for the investigated 3d transition metals in Ge. For the near-BC site, the obtained fractions are all between $22 \pm 1\%$ and the lower detection limit of the emission channeling technique. For the investigated impurities, no fractions on the near-BC site are present after a particular annealing temperature (600°C, 400°C, 500°C and 350°C for Mn, Fe, Ni and Cu in Ge respectively). It is interesting to note that Fe and Cu atoms on the S site have a higher thermal stability compared to the near-BC site (i.e. Ni atoms on the S site can still be observed above the temperature at which the near-BC site is annealed). This is in contrast to the Mn and Ni atoms in Ge, where both fractions on the S and near-BC site are annealed in the same temperature range.

Similarities between the investigated 3d transition metals in Ge about the occupied lattice site are observed in figure 3.6. First of all, apart from the substitutional site also interstitial sites are present. The S site is stable up to at least 350°C and the near-BC site up to 300°C. The fraction of transition metals on the S site and on the near-BC location varies between 20% and 40% and between 20% and 30% respectively. In some cases the fractions of impurities occupying the substitutional sites are larger than the ones on interstitial locations, while in other cases, the situation is reversed. However, it is very difficult to find an unequivocal interpretation of such small differences, since the number of produced defects depends on the implantation parameters (temperature, fluence), which are not necessarily the same for the different experiments. For example, in order for impurities to occupy the BC site, which is related to a split-vacancy configuration, the presence of vacancies is required.

Nevertheless, Ni is a very special case. Apart from the near-BC site, also a T site with a large rms displacement is present. From this point of view, it is important to note that the enlarged simulation set (containing simulations for different large rms displacements around the T sites) was only used in the analysis of the Ni experiment. Although the previous emission channeling experiments on other 3d transition metals did not show obvious indications of a third lattice site (in addition to S and BC), it would be interesting to re-analyze the data with an equivalent enlarged simulation set containing the displaced T sites. In addition, annealing steps at higher temperatures would be required for the Fe and Cu experiments, in order to allow for a better understanding of the thermal stability of the different occupied lattice sites.

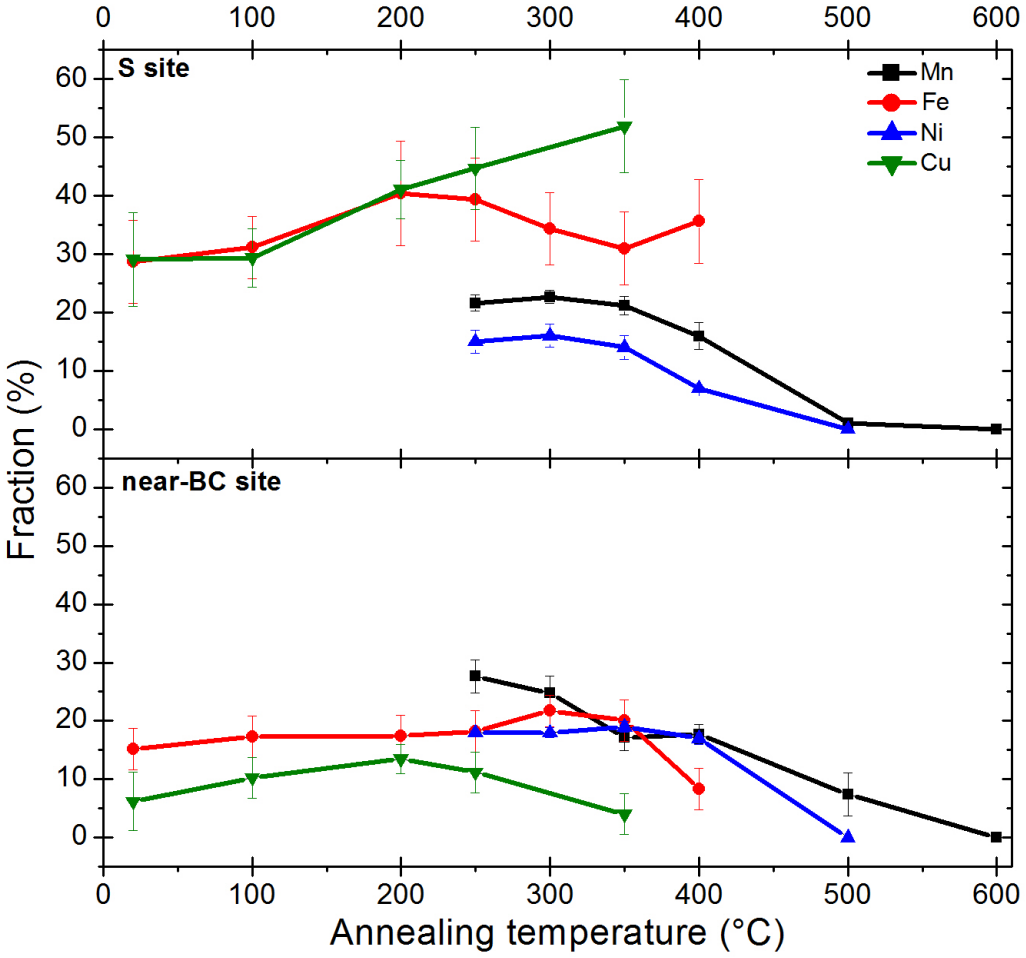

FIGURE 3.5: Comparison of the fitted fractions on the S and near-BC sites in function of particular annealing temperatures of different transition metals (Mn, Fe, Ni and Cu) in Ge. Data for Fe and Cu in Ge is reported by Decoster *et al.* [40].

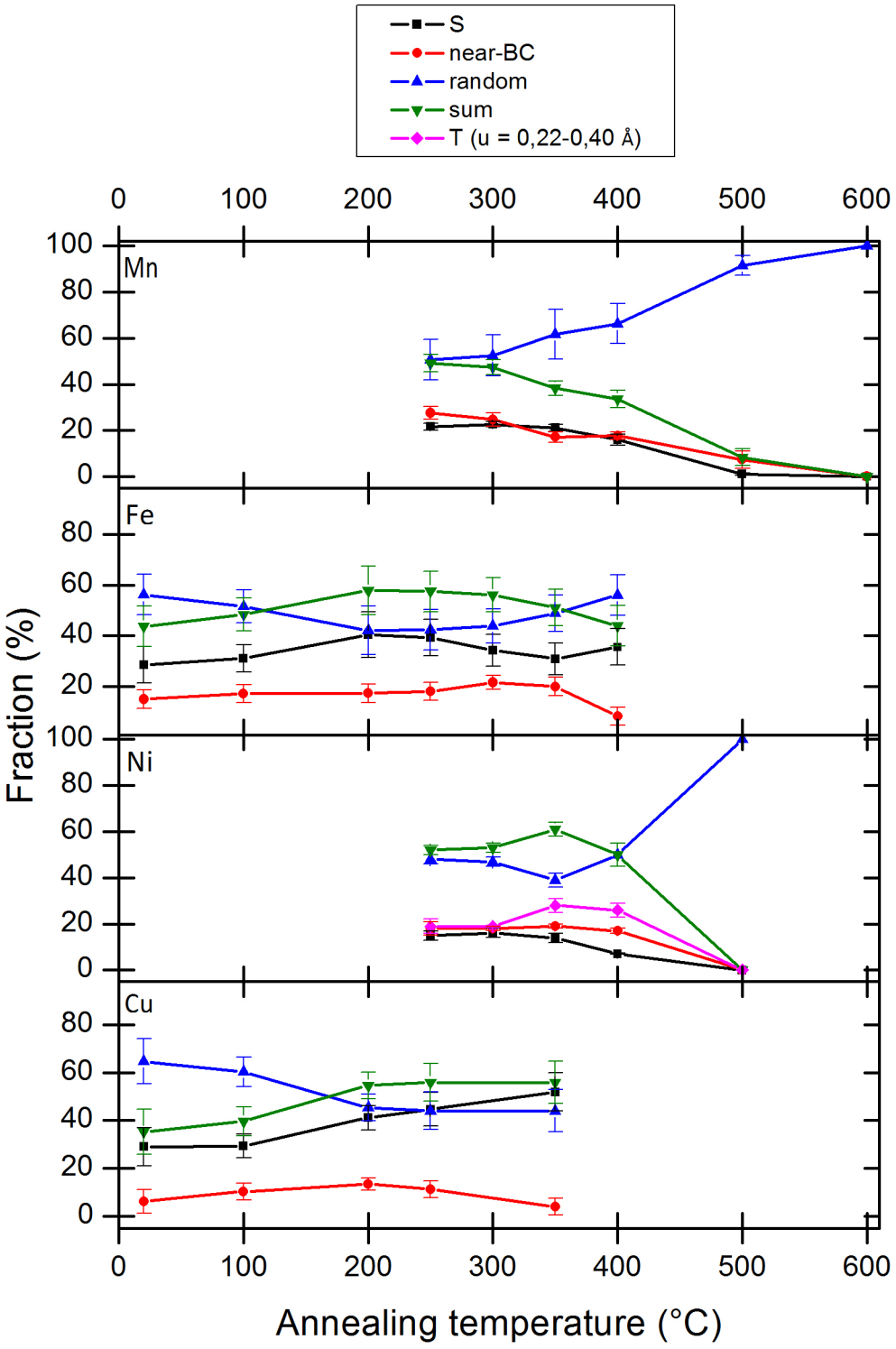

FIGURE 3.6: Comparison of the fitted fractions as a function of particular annealing temperatures of different transition metals (Mn, Fe, Ni and Cu) in Ge. Data for Fe and Cu in Ge is reported by Decoster *et al.* [40].

Isotope	mass (a.m.u.)	energy (keV)	implantation temperature (°C)	R_p (Å)	$f_{E,vac}$ (%)	number of vacancies per ion	tilt angle (°)	maximal fluence (atoms/cm^2)	peak concentration (atoms/cm^3)	nearest impurity distance (Å)
^{56}Mn	55.94	40	250	258	7.06	1394	17	$1.3 \cdot 10^{12}$	$3.38 \cdot 10^{17}$	143
^{56}Mn	55.94	50	300	313	6.98	1726	17	$6.8 \cdot 10^{11}$	$1.56 \cdot 10^{17}$	186
^{56}Mn	55.94	60	RT	364	6.92	2053	17	$6.7 \cdot 10^{11}$	$1.34 \cdot 10^{17}$	195
^{65}Ni	64.93	30	250	191	7.44	1106	17	$1.5 \cdot 10^{12}$	$5.55 \cdot 10^{17}$	122

TABLE 3.1: Overview of the implantation details for the used radioactive isotopes: mass, energy, implantation temperature (RT = room temperature), mean projected range or longitudinal range, fraction of the total ion energy converted in vacancy creation, number of created vacancies before the annealing steps, the tilt angle between the sample normal and the ion beam, the maximal fluence or dose, the peak impurity concentration and the distance between two nearest impurity neighbours. The calculations are done in the Monte Carlo simulation program SRIM (version 2013) [65], with a Ge displacement threshold of 15 eV and a lattice binding energy of 2 eV.

Isotope	energy (keV)	implantation temperature (°C)	maximal fluence (atoms/cm^2)
^{56}Mn	40	250	$1.3 \cdot 10^{12}$
^{59}Fe	60	RT	$6.6 \cdot 10^{12}$
^{65}Ni	30	250	$1.5 \cdot 10^{12}$
^{67}Cu	60	RT	$1.0 \cdot 10^{13}$

TABLE 3.2: Implantation related properties of the executed electron emission channeling experiments for transition metals (Mn, Fe, Ni and Cu) in Ge. Data for Fe and Cu in Ge is reported by Decoster *et al.* [40]. RT means room temperature.

Chapter 4

Conclusions and outlook

In conclusion, the lattice site location as a function of annealing temperature was investigated after the ion implantation of transition metals in germanium. It is crucial to know the (thermal stability of) the exact lattice site, which was obtained by using the emission channeling technique, since they determine the functional properties (e.g. electrical and magnetic) of doped semiconductors.

Apart from the occupation of substitutional (S) sites, all investigated 3d transition metals in Ge until now (Mn, Fe, Ni and Cu) exhibit a fraction on the bond-centered (BC) site, which is a high symmetry site in between two nearest neighbouring S sites (along the $< 111 >$ direction). This site is occupied when an impurity on the substitutional site traps a vacancy, whereby the transition metal will end up in a split-vacancy configuration. Therefore, the occupation of the BC site is related to the presence of vacancies in the sample. These vacancies are abundantly available as a consequence of the implantation process. Nevertheless, Ni was a special case. Apart from the BC site, another interstitial site was occupied as well: a fraction of the Ni atoms are located on a tetrahedral (T) site with a large rms displacement. The occupation of this T site is believed to be related to defects introduced by ion implantation.

The lattice sites were determined both immediately after implantation as well as after annealing at different temperatures. For the previously investigated 3d transition metals in Ge, i.e. Fe and Cu, the S and the near-BC site were stable up to 350°C and 300°C respectively. Moreover, Ni atoms occupied T sites up to an annealing temperature of 400°C.

As an outlook, these results motivate further research on the lattice location of Ni in Ge, in particular because the occupation of the T site has not completely understood yet. Although the configuration of the defect-related T site is not known, ab initio calculations about the heat of formation to occupy a particular site or complex could be helpful. In general, more investigations are needed on diffusion coefficients of transition metals in Ge (especially under the same experimental conditions), because the calculations of these coefficients do not take into account implantation related defect complexes.

Secondly, for the experiments of Fe and Cu in Ge, the analysis should be redone by using the enlarged simulation set which also allows the occupation of the T site with varying thermal vibration amplitudes (this site was not taken into account in the previous analysis).

Finally, since a significant difference between 3d transition metals is found, it would be interesting to investigate cobalt (Co) in Ge as well, whereby all the 3d transition metals between Mn and Cu can be compared (see figure 4.1).

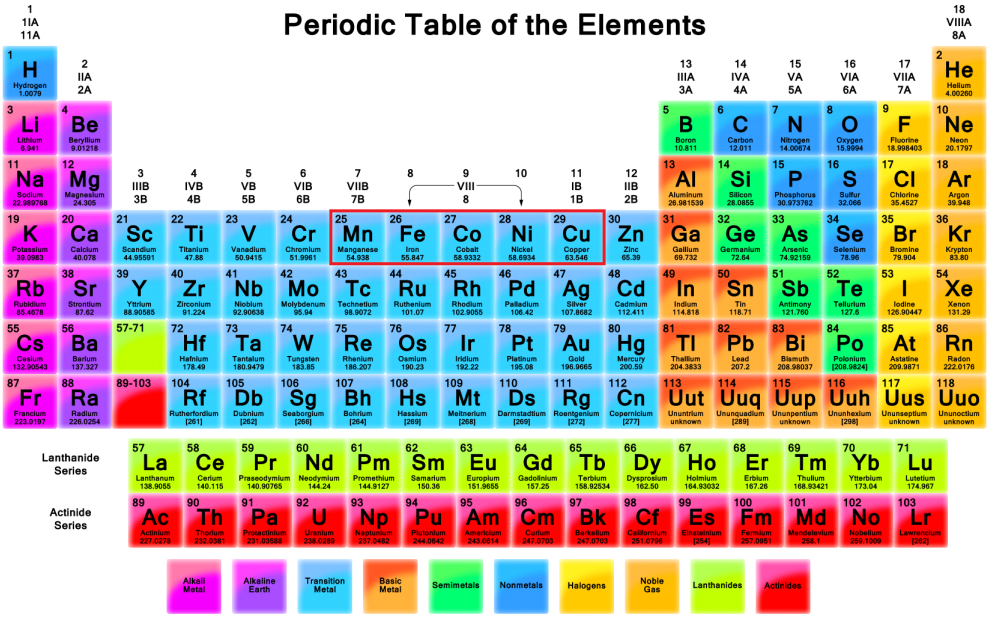

FIGURE 4.1: Periodic table.

Bibliography

[1] H. Winkler, "Mittheilungen über das Germanium," *J. Prak. Chemie*, vol. 34, p. 117, 1886.

[2] E. Simoen and C. Claeys, *Germanium-based technologies: from materials to devices*. Amsterdam: Elsevier, 2007.

[3] G. Teal, M. Sparks, and E. Buelher, "Single-crystal germanium," *Proc. I.R.E.*, vol. 40, p. 906, 1952.

[4] K. Prabhakaran and T. Ogino, "Oxidation of Ge(100) and Ge(111) surfaces: an UPS and XPS study," *Surf. Sci*, vol. 325, p. 263, 1995.

[5] E. Schubert, "Silicon versus germanium - a historical perspective," http://www.ecse.rpi.edu/~schubert/Course-Teaching-modules/A027-Silicon-versus-germanium---A-historical-perspective.pdf, 2011.

[6] M. Separation, "Motorola Automotive Legacy," http://direct.motorola.com/ENS/T805/site/motolegacy.html, 2011.

[7] J. Kilby, "Invention of the integrated circuit," *IEEE Trans. Electron Dev.*, vol. 23, p. 648, 1976.

[8] R. Hull and J. Bean, *Germanium Silicon: Physics and Materials, Semiconductors and Semimetals*. San Diego: Academic, 1999.

[9] G. Knoll, *Radiation detection and measurement*. United States of America: John Willey & Sons, 2000.

[10] D. Bode and H. Graham, "A comparison of the performance of copper-doped germanium and mercury-doped germanium detectors," *Infrared Physics*, vol. 3, p. 129, 1963.

[11] S. Gaudet, C. Detavernier, A. Kellock, P. Desjardins, and C. Lavoie, "Thin film reaction of transition metals in germanium," *J. Vac. Sci. Technol. A*, vol. 24(3), p. 474, 2006.

[12] L. Pereira, U. Wahl, S. Decoster, j.G. Correia, L. Amorim, M. da Silva, J. A. ujo, and A. Vantomme, "Stability and diffusion of interstitial and substitutional Mn in GaAs of different doping types," *Phys. Rev. B*, vol. 86, p. 125206, 2012.

[13] C. Kittel, *Introduction to solid state physics*. London: John Willey & Sons, 1953.

[14] W. Tyler, "Deep level impurities is germanium," *J. Phys. Chem. Solids*, vol. 8, p. 59, 1959.

[15] H. Woodbury and W. Tyler, "Properties of germanium doped with manganese," *Phys. Rev.*, vol. 100(2), p. 659, 1955.

[16] W. Tyler, R. Newman, and H. Woodbury, "Properties of germanium doped with nickel," *Phys. Rev.*, vol. 98(2), p. 461, 1955.

[17] S. Decoster, "Ion implantation in Ge: structural and electrical investigation of the induced lattice damage and study of the lattice location of implanted impurities," Phd thesis, Katholieke Universiteit Leuven, 2009.

[18] J. Araújo, K. Bharuth-Ram, J. Correia, M. da Silva, S. Decoster, B. D. Vries, H. Hofsäss, T. Mendonç, C. R. L. Pereira, J. Soares, A. Vantomme, and U. Wahl, "Emission channeling lattice location experiments with short-lived isotopes (2006)," *Proposal to the isolde and neutron time-of-flight experiments committee (INTC)*, 2006.

[19] Nature publishing group, "Nature materials inside, spintronics," *Nature*, vol. 11, p. 063712, 2012.

[20] S. Zhou and H. Schmidt, "Mn-doped Ge and Si: a review of the experimental status," *Materials*, vol. 3, p. 5054, 2010.

[21] A. Ural, P. Griffin, and J. Plummer, "Self-diffusion in silicon: similarity between the properties of native point defects," *Phys. Rev. Lett.*, vol. 83, p. 3454, 1999.

[22] A. Fazzio, A. Janotti, and A. da Silva, "Microscopic picture of the single vacancy in germanium," *Phys. Rev. B*, vol. 61, p. R2401, 2000.

[23] A. Giese, N. Stolwijk, and H. Bracht, "Double-hump diffusion profiles of copper and nickel in germanium wafers yielding vacancy-related information," *Appl. Phys. Lett.*, vol. 77(5), p. 642, 2000.

[24] G. Vogel, G. Hettich, and H. Mehrer, "Self-diffusion in intrinsic germanium and effects of doping on self-diffusion in germanium," *J. Phys. C: Solid State Phys.*, vol. 16, p. 6197, 1983.

[25] M. Werner, H. Mehrer, and H. Hochheimer, "Effect of hydrostatic pressure, temperature, and doping on self-diffusion in germanium," *Phys. Rev. B*, vol. 32, p. 3930, 1985.

[26] A. Portavoce, O. Abbes, Y. Rudzevich, L. Chow, V. L. Thanh, and C. Girardeaux, "Manganese diffusion in monocrystalline germanium," *Scripta Materialia*, vol. 67, p. 269, 2012.

[27] L. Wei, "Diffusion of silver, cobalt and iron in germanium," *J. Phys. Chem. Solids*, vol. 18, p. 162, 1961.

[28] F. Frank and D. Turmbull, "Mechanisms of diffusion of copper in germanium," *Phys. Rev.*, vol. 104, p. 617, 1956.

[29] F. van der Maesen and J. Brenkman, "On the behaviour of rapidly diffusing acceptors in germanium," *J. Electrochem. Soc.*, vol. 102, p. 229, 1955.

[30] H. Bracht, N. Stolwijk, and H. Mehrer, "Diffusion and solubility of copper, silver and gold in germanium," *Phys. Rev. B*, vol. 43, p. 14465, 1991.

[31] A. Giese, H. Bracht, N. Stolwijk, and H. Mehrer, "Diffusion of nickel and zinc in germanium," *Defect and diff. forum*, vol. 143(2), p. 1059, 1997.

[32] R. Hall, "Variation of the distribution coefficient and solid solubility with temperature," *J. Phys. Chem. Solids.*, vol. 3, p. 63, 1957.

[33] F. Trumbore, "Solid solubilities of impurity elements in Ge and Si," *The bell system technical journal*, 1960.

[34] A. Continenza, G. Profeta, and S. Picozzi, "Transition metal impurities in Ge: Chemical trends and codoping studied by electronic structure calculations," *Phys. Rev. B*, vol. 73, p. 35212, 2006.

[35] S. Decoster, U. Wahl, S. Cottenier, J. Correia, T. Mendonça, L. Amorim, L. Pereira, and A. Vantomme, "Lattice position and thermal stability of diluted As in Ge," *Appl. Phys. Lett.*, vol. 111, p. 53528, 2012.

[36] U. Wahl, J. Correira, A. Vantomme, G. Langouche, and the ISOLDE collaboration, "Lattice location of implanted Cu in Si," *Physica B*, vol. 273-273, p. 367, 1999.

[37] P. Clauws and E. Simoen, "Metals in germanium," *Mat. Sci. Semicond. Proc.*, vol. 9, p. 546, 2006.

[38] P. Clauws, J. V. Gheluwe, J. Lauwaert, E. Simoen, J. Van-hellemont, M. Meuris, and A. Theuwis, "Deep level transient spectroscopy of transition metal impurities in germanium," *Physica B*, vol. 401, p. 188, 2007.

[39] E. Simoen, K. Opsomer, C. Claeys, K. Maex, C. Detavernier, R. V. Meirhaeghe, and P. Clauws, "Study of metal-related deep level defects in germanide Schottky barriers on n-type germanium," *J. Appl. Phys.*, vol. 104, p. 23705, 2008.

[40] S. Decoster, S. Cottenier, B. D. Vries, H. Emmerich, U. Wahl, J. Correia, and A. Vantomme, "Transition metal impurities on the bond-centered site in germanium," *Phys. Rev. Lett.*, vol. 102, p. 65502, 2009.

[41] U. Wahl, J. Correia, J. Soares, and the ISOLDE Collaboration, "Lattice location and stability of implanted Cu in Ge," *Physica B*, vol. 340, p. 799, 2003.

[42] H.P. Gunnlaugsson AND G. Weyer AND M. Dietrich AND M. Fanciulli AND K. Bharuth-Ram and R. Sieleman AND (ISOLDE Collaboration), "Mössbauer spectroscopy on Fe impurities in germanium," *Physica B*, vol. 340-342, p. 537, 2003.

[43] J. Mayer, L. Eriksson, and J. Davies, *Ion implantation of semiconductors*. New York: Academic Press, 1970.

[44] T. Haynes and O. Holland, "Comparative study of implantation-induced damage in GaAs and Ge: temperature and flux dependence," *Appl. Phys. Lett.*, vol. 59, p. 452, 1991.

[45] S. Sigurd, G. Fladda, L. Eriksson, and K. Björkqvist, "Lattice disorder in Ge by boron ion bombardment," *Radiat. Eff.*, vol. 3, p. 145, 1970.

[46] B. Appleton, O. Holland, J. Narayan, O. Schow, J. Williams, K. Short, and E. Lawson, "Characterization of damage in ion implanted Ge," *Appl. Phys. Lett.*, vol. 41(8), p. 711, 1982.

[47] S. Decoster and A. Vantomme, "Implantation-induced damage in Ge: strain and disorder profiles during defect accumulation and recovery," *J. Phys. D: Appl. Phys.*, vol. 42, p. 165404, 2009.

[48] C. Emtsev, T. Mashovets, V. Mikhnovich, and N. Vitosvkii, "Frenkel pairs in silicon and germanium," *Radiat. Eff. Defects Solids*, vol. 99, p. 111, 1989.

[49] H. Höfler, N. Atodiresei, K. Schroeder, R. Zeller, and P. Dederichs, "Impurity-vacancy complexes in Si and Ge," *Hyperfine interactions*, vol. 158, p. 37, 2004.

[50] S. Cottenier, "WIEN2K," http://www.wien2k.at/reg_user/textbooks, 2001, [ISBN 90-807215-1-4].

[51] P. Blaha, K. Schwarz, G. Madsen, D. Kvasnicka, and J. Luitz, *Wien2K: An augmented plane wave pluc local orbitals program for calculating crytal properties*. Austria: Karlheinz Schwarz, Techn. Universität Wien, 2001.

[52] S. Decoster, S. Cottenier, U. Wahl, J. Correia, and L. P. et al., "Diluted manganese on the bond-centered site in germanium," *Appl. Phys. Lett.*, vol. 97, p. 151914, 2010.

[53] H. Haesslein, R. Sielemann, and C. Zistl, "Vacancies and Self-interstitials in Germanium Observed by Perturbed Angular Correlation Spectroscopy," *Phys. Rev. B*, vol. 80(12), p. 2626, 1997.

[54] U. Wahl, *Emission channeling: charged particle-solid interactionm detection and lattice location methods (Script to accompany a Masters course on this subject)*. Sacavém, Portugal: Instituto Tecnológico e Nuclear, 2006.

[55] B. N. L. National Nuclear Data Center, "NuDat 2.6," http://www.nndc.bnl.gov/nudat2/.

[56] W.H. Bragg, "The consequence of the corpuscular hypothesis of the α and X rays, and the range of β rays ," *Philosophical Magazine*, vol. 20, pp. 385–416, 1910.

[57] L.C. Feldman and J.W. Mayer, *Fundamentals of surface and thin film analysis*. New York: North-Holland, 1986.

[58] J. Lindhard, "Influence of crystal lattice on motion of energetic charged particles," *Mat. Fys. Medd. Dan. Vid. Selsk.*, vol. 34, p. 14, 1965.

[59] B. D. Vries, "Lattice site location of impurities in group III nitrides using emission channeling," Phd thesis, Katholieke Universiteit Leuven, 2006.

[60] L. Amorim, J. Araújo, K. Bharuth-Ram, J. Correia, V. Darakchieva, M. da Silva, S. Decoster, H. Hofsäss, M. Nagl, L. Pereira, A. Vantomme, U. Vetter, and U. Wahl, "Emission channeling lattice location experiments with short-lived isotopes (2010)," *Proposal to the isolde and neurton timeo-of-flight experiments committee (INTC); status report and addendum to experiment IS453*, 2010.

[61] P. Van Duppen, "Isotopes separation on line and post acceleration," *Lect. Notes Phys.*, vol. 700, pp. 37–77, 2006.

[62] ISOLDE Corporation, "General overview of ISOLDE complex," http://ab-dep-op-iso.web.cern.ch/ab-dep-op-iso/HTML/hall_overview.htm.

[63] U. Wahl, J. Correia, A.Czermak, S.G.Jah, J. P.Jalocha, A. Ridge, F. Schopper, J. Soares, and A. Vantomme, "Position sensitive Si pad detectors for electron emission channeling experiment," *Nucl. Instr. And Meth. in Phys. Rev. A*, vol. 524, pp. 245–256, 2004.

[64] H. ass and G. Lindner, "Emission channeling and blocking," *Phys. Rep.-Rev. Sec. Phys. Lett.*, vol. 3201, p. 121, 1991.

[65] J. Ziegler, J. Biersack, and U. Littmark, *The stopping and range of ions in solids*. New York: Pergamon Press, 1985.

[66] J. Beirlant, G. Dierkx, and M. Hubert, *Statistiek en wetenschap*. ACCO, 2005.

[67] S. Agostinelli *et al.*, "Geant4 - a simulation toolkit," *Nucl. Instr. And Meth. A*, vol. 506, p. 250, 2003.

[68] S. Estreicher, M. Sanati, and N. G. Szwacki, "Iron in silicon: Interactions with radiation defects, carbon and oxygen," *Phys. Rev. B*, vol. 77, p. 125214, 2008.

[69] S. Decoster, B. D. Vries, U. Wahl, J. Correia, and A. Vantomme, "Experimental evidence of tetrahedral interstitial and bond-centered Er in Ge," *Appl. Phys. Lett.*, vol. 93, p. 141907, 2008.

[70] U. Wahl, A. Vantomme, and G. Langouche, "Lattice location and stability of ion implantated Cu in Si," *Phys. Rev. Lett.*, vol. 84(7), p. 1495, 2000.

INSTITUUT VOOR KERN-EN STRALINGSFYSICA
Celestijnenlaan 200D
3001 LEUVEN, BELGIË
tel. + 32 16 32 72 63
fax + 32 16 32 79 85
http://fys.kuleuven.be/iks